ADAPTIVE RESONANT MODE ACTIVE NOISE CONTROL

by

Adam K. Smith

BS, University of Pittsburgh, 2003

Submitted to the Graduate Faculty of

the School of Engineering in partial fulfillment

of the requirements for the degree of

Master of Science

University of Pittsburgh

2005

UNIVERSITY OF PITTSBURGH

SCHOOL OF ENGINEERING

This thesis was presented

by

Adam K. Smith

It was defended on

October 12, 2005

and approved by

Jeffrey S. Vipperman, Associate Professor, Mechanical Engineering Department

Daniel D. Budny, Associate Professor, Civil and Environmental Engineering Department

William W. Clark, Professor, Mechanical Engineering Department

Thesis Advisor: Jeffrey S. Vipperman, Associate Professor, Mechanical Engineering Department

ABSTRACT

ADAPTIVE RESONANT MODE ACTIVE NOISE CONTROL

Adam K. Smith, MS

University of Pittsburgh, 2005

Low frequency sound waves propagating in a duct is ideally suited for active noise control (ANC) applications. Unlike passive treatments, ANC utilizes an acoustic actuator (loudspeaker) to cancel unwanted sound fields. There are two main control topologies when considering the active suppression of sound, feedforward and feedback. The former requires that the disturbance be known before the control signal is generated, and is ideal for periodic or random signals. Feedback arrangements, on the other hand, modify the dynamics of an enclosured sound field to augment damping, and requires no *a priori* knowledge of the disturbance. A modified version of feedback that is used in structures called positive position feedback (PPF), can be applied to acoustic systems. In a previous study, a tuned resonant filter modelled after a Helmholtz resonator was used in PPF configuration to suppress noise levels by Bisnette and Vipperman (2004). However, the presence of speaker dynamics necessitates further phase compensation, which is accomplished with an all-pass filter. The work presented here further develops this control method by using a higher-order compensator. In this study, band-pass filters are used to improve the multi-modal control by limiting phase interaction of adjacent modes. Further refinements are made by realizing the control system electronically, which gives the ability to adapt controller parameters. Here, an algorithm is presented that adapts the resonant controller gain. Experimental results show moderate reductions with no energy spill-over to the next adjacent uncontrolled mode.

TABLE OF CONTENTS

1.0 INTRODUCTION 1

2.0 THEORETICAL DEVELOPMENT 7

2.1 ANALYTICAL DUCT MODEL 7

2.1.1 Acoustic Enclosure 8

2.1.2 Acoustic Actuator 9

2.2 UNCONTROLLED SYSTEM 10

3.0 CONTROL SIMULATION 12

3.1 CONTROL SYSTEM CONFIGURATION 13

3.2 COMPENSATOR DESIGN 14

3.2.1 Resonant Compensating Filter 16

3.2.2 Phase Compensation 20

3.3 SINGLE MODE CONTROL 21

3.4 MULTIPLE MODE CONTROL 25

4.0 EXPERIMENTAL DEMONSTRATION 29

4.1 SINGLE MODE CONTROL 31

4.1.1 Collocated Control 32

4.1.2 Non-Collocated Control 35

4.2 MULTIPLE MODE CONTROL 38

5.0 ADAPTIVE CONTROL 43

5.1 PRELIMINARY ADAPTIVE ALGORITHM 44

5.2 ADAPTIVE CONTROL SIMULATION 48

5.3 EXPERIMENTAL ADAPTIVE CONTROL DEMONSTRATION 49

6.0 CONCLUSIONS AND FUTURE WORK 52
APPENDIX A. MATLAB SIMULINK™ CODE FOR ADAPTIVE CONTROL SIMULATIONS 55
APPENDIX B. MATLAB SIMULINK™ CODE FOR ADAPTIVE CONTROL EXPERIMENTAL DEMONSTRATION 58
BIBLIOGRAPHY 60

LIST OF TABLES

1 Plant parameters used in simulation. 11
2 Source loading measurements. 32
3 First 4 pressure nodes of the acoustic duct. 38

LIST OF FIGURES

1 Block diagram of PPF control. 3
2 Frequency response of PPF control. 4
3 Uncontrolled and controlled frequency response of PPF control. 6
4 Acoustic duct setup. 7
5 Simulated and experimental results for uncontrolled system. 10
6 Schematic of system conventions. 13
7 Transfer function paths for duct test bed. 14
8 FRF of uncontrolled control/sensor transfer function path. 16
9 FRF of control/sensor path with band-pass (left) and low-pass (right) filters. 17
10 Frequency response of 2^{nd}-order band-pass resonant filter. 18
11 Comparison of 4^{th}-order digital filters for first mode control. 19
12 Nyquist plot of control/sensor path with and without phase compensation. . . 22
13 Comparison of different order Chebyshev controller responses. 24
14 Simulated control comparison with 4^{th}-order control filters. 24
15 Magnitude response of the disturbance/sensor path for 3 single-mode controls. 25
16 FRF of 4^{th}-order band-pass filters on the simulated control/sensor path. . . . 26
17 Simulated comparison of different order Elliptic compensator responses. . . . 27
18 Simulated comparison of multi-modal Butterworth, Chebyshev, and Ellipitical controller responses. 28
19 FRF of simulated disturbance/performance path showing 4-mode control. . . 28
20 Picture of the experimental acoustic duct. 30
21 Measurement ports along the acoustic duct. 30

22 FRF of the experimental control/sensor path. 33
23 Experimental comparison of different order Elliptic controller responses. . . . 34
24 Experimental comparison of different design-type 4^{th}-order filter responses. . 35
25 Single mode uncontrolled vs. controlled disturbance/performance path response. 36
26 1^{st} mode response along duct axis. 37
27 Non-collocated uncontrolled vs. controlled disturbance/performace path. . . . 37
28 FRF of experimental control/sensor path with and without 4^{th}-order band-pass filters. 39
29 Experimental comparison of different order Chebyshev controller responses. . 40
30 Experimental comparison of multi-modal Butterworth, Chebyshev, and Elipitical controller responses. 41
31 FRF of experimental multi-modal uncontrolled vs controlled disturbance/performance path. 42
32 1^{st} through 4^{th} mode reductions in response along duct axis. 42
33 Flow diagram of the adaptive algorithm. 45
34 Root locus plot of 4-mode controller on the control/sensor path 46
35 Block diagram of the adaptive feedback controller. 47
36 Uncontrolled and adaptively controlled disturbance/sensor signal. 48
37 Response of adaptive uncontrolled and controlled disturbance/performance path. 49
38 Experimental uncontrolled vs adaptively controlled disturbance/performance response. 51
39 Simulink code for the simulated adaptively controlled system. 55
40 Simulink code for the simulated acoustic duct sub-system. 56
41 Simulink code for the simulated adaptive algorithm sub-system. 56
42 Simulink code for the simulated controller sub-system. 57
43 Simulink code for the experimental adaptive controller. 58
44 Simulink code for the experimental adaptive algorithm sub-system. 59

NOMENCLATURE

Symbols

l : Length

w : Width

h : Height

V : Volume of duct

A : Area of speaker cone

x : Position

R : Resistance

L : Inductance

C : Capacitance, or Cost function

I : Current

m : Mass of loudspeaker cone

b : Damping ratio of loudspeaker

k : Stiffness of loudspeaker

Bl : Electro-mechanical coupling coefficient

c : Sound speed in air

N : Number of modes

t : Time

f : Frequency

$v(t)$: Applied voltage

$y(t)$: Speaker displacement function

$p(x,t)$: Pressure function

H : Transfer function

s : Laplace variable

K : Filter gain

Δk: gain increment

z : Filter zero

p : Filter pole

μ : State variable

φ : State output vector

ρ_o : Density of air at room temperature

Ψ : Eigenfunction of duct

ϕ : Structural/acoustical coupling coefficient

β : State duct model input coefficients

γ : State duct model pressure output coefficents

ω : Circular frequency

ζ : Damping ratio

θ : Phase angle

P : Performance measurement port

Δx : Measurement port distance

$e(n)$: Error signal

$u(n)$: Control signal

$d(n)$: Disturbance signal

$s(n)$: sensor signal

Subscripts

n : Mode index, or referring to noise speaker

j : Speaker index

co : Cuttoff frequency

d : Referring to duct

s : Referring to loudspeaker

$perf$: Referring to performance signal

sen : Referring to sensor signal

$dist$: Referring to disturbance signal

$cont$: Referring to control signal

dp : Referring to distrubance/performance path

ds : Referring to distrubance/sensor path

cs : Referring to control/sensor path

cp : Referring to control/performance path

c : Referring to control speaker

$comp$: Referring to the compensator

f : Referring to generic filter

a : Referring to all-pass filter

g : Referring to gain circuit

LP : Low-pass filter

BP : Band-pass filter

AP : All-pass filter

Superscripts

$\dot{}$: First derivative, $\frac{d}{dt}$

$\ddot{}$: Second Derivative, $\frac{d^2}{dt^2}$

1.0 INTRODUCTION

There are two distinct means to abate unwanted sound, passive and active. Passive noise control can be accomplished by adding absorptive treatments to surfaces, or fabricating barriers or enclosures. For example, foam insulation and ceiling tiles have become features at many offices to dissipate or disrupt the reflection of the sound field. The size and density of passive treatments are dependent upon the acoustic wavelength, making them ideal for middle to high frequency noise applications. Active Noise Control (ANC) uses the principle of destructive interference of waves to attenuate undesired noise. An acoustic actuator (loudspeaker) is used to produce a signal that is "out of phase" with the disturbance. Active approaches work best when the wavelength is long compared to the dimensions of its surroundings, i.e. low frequencies noise in a waveguide. Both passive and active noise control can be used individually, or to complement one another [1, 18].

An exception to passive devices not working well at low frequencies is the Helmholtz resonator. For example, when the dimensions of an acoustic system are small in comparison to the wavelength of the disturbance, the motion of the medium is analogous to lumped parameter mechanical system [17]. The enclosed volume of air acts as a spring connected to the mass of the slug of air, and vibrates at a frequency dependent on the density and volume of the air and the mass of the slug of air in the neck. To obtain noise suppression, the natural frequency of the device is tuned to match the targeted control frequency. The radiation of sound into the surrounding medium leads to the dissipation of acoustic energy, which acts as resistance element at the opening. Helmholtz resonators can be used to remove energy at single or multiple frequencies. These devices have been implemented in a host of applications, such as buildings, acoustic barriers, rocket fairings, and mufflers. The damping of a Helmholtz resonator, much like vibration absorbers, determines the amount of control

that is to be expected [5, 8]. Due to the sensitivity of acoustic systems, a disadvantage of using these devices is their inability to modify the fixed natural frequency. Approaches have been developed to physically adapt the mechanical tuning of Helmholtz resonators [15, 18, 25]. However, due to the active component implementing the tuning of the resonator, these methods can be unwieldily and have physical limitations.

There are two distinct approaches to ANC: feedforward and feedback. Feedforward control uses a coherent reference to form the control signal that drives an acoustic actuator. Most feedforward techniques employ an adaptive algorithm, where the performance of the controller is measured by an error sensor. This measurement provides a signal that an algorithm uses to update the controller. For example, a least-mean-square (LMS) algorithm updates the coefficients of a finite impulse response (FIR) filter controller to minimize mean-squared error. An inherent requirement of feedforward systems is that the signal processing time be less than the time it takes sound to propagate from the reference to the error sensor [14]. It should be noted that as the error signal is minimized, higher gains will be required for the controller, making a less stable system. Despite these drawbacks feedforward ANC is a widely applicable control system arrangement that has shown great ability to attenuate disturbances [25, 26].

While feedforward systems require a knowledge of the incoming disturbance to generate an "anti-noise" signal, feedback systems attenuate the disturbance as it occurs. Thus, feedback approaches are often better at diminishing transient events. Feedback approaches change the system response by adding damping and modifying the resonant frequencies. A feedback control scheme uses a sensor to detect the disturbance, and formulates a suitable control signal that drives a loudspeaker. The best known example of feedback ANC is active ear muffs (or active headset) [11]. The acoustic disturbance is attenuated at a microphone inside the headset, effectively creating a zone of silence at the user's ear. It is required that the location of the disturbance sensor be in close proximity to the acoustic actuator for feedback systems. The distance between actuator and sensor determines the system delay, which is proportional to the effective bandwidth of the controller [14].

Vibrating structures, as with acoustic systems, have modes in which vibration occurs, and the strongest oscillation occurs at the systems resonant frequencies. Although similar

in some respects, feedback control of structural and acoustic systems have important differences. Structural feedback systems can achieve perfect collocation between the sensor and actuator pair [9], whereas acoustic feedback systems can not [3]. The sensor (microphone) and actuator (loudspeaker) for acoustic systems can only achieve a "substantially collocated" transducer pair, by placing the sensor at the center of the loudspeaker's face. However, the loudspeaker adds significant dynamics to the system which can cause instability and erode controller performance.

An unconventional yet simple control approach that is used for large space structures is positive position feedback (PPF) [9, 12]. As shown in Figure 1, the control signal is formed by feeding back structure displacement (ξ) through a damped resonant (low-pass) filter, whose displacement (η) is fed back through a positive gain, to form the feedback signal. The corner frequency (ω_c) of the compensator is tuned to the resonant frequency of the structure. Figure 2 shows the response of implementing PPF on a single degree of freedom system. By examining open-loop combined phase contribution of the system (solid line) and low-pass filter (dashed line), it can be seen that a signal is produced (dash-dot line) that is 180^o at ω_c. The magnitude response of Figure 2 shows the attenuation that occurs when the system and low-pass filter are combined. The control path is guaranteed to be minimum-phase due to the collocation of sensor/actuator pair (i.e. peizoceramic patches), which are free of dynamics at low frequencies.

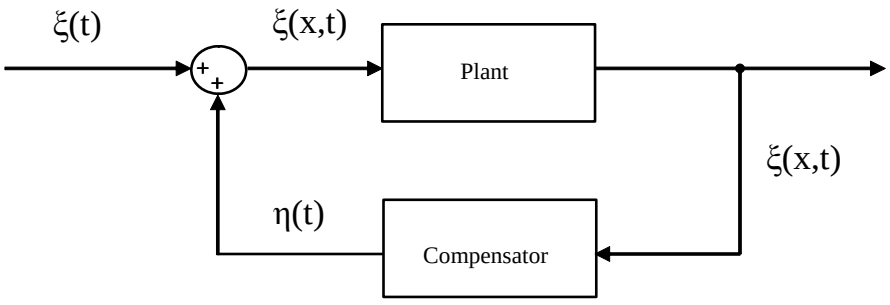

Figure 1: Block diagram of PPF control.

A Helmholtz resonator could be used as the compensating filter for PPF of an acoustic system. These devices can be modeled as a 2^{nd}-order electrical system using analog circuit components [17]. Realizing a Helmoltz resonator as either a low-pass or band-pass filter enables PPF to be extended to acoustic systems [3]. Furthermore, electronically realized Helmholtz resonators provides more flexibility in the design process and easier adaptation. Unlike its physical counterpart, an electronically realized Helmholtz resonator could control multiple acoustic modes on the same hardware (i.e loudspeaker, microphones, digital signal processor), and allow for easy changing of resonator parameters. Thus, PPF can provide a stable, attenuating response that is analogous to a tuned absorber.

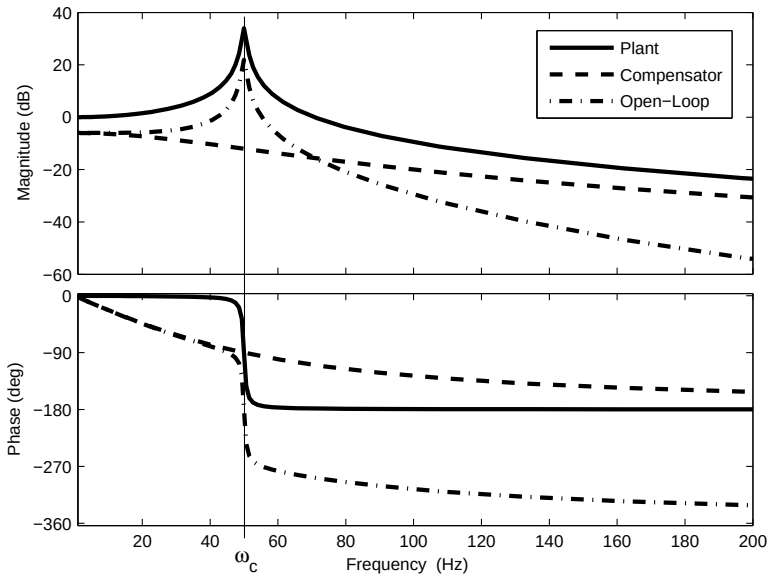

Figure 2: Frequency response of PPF control.

ANC systems utilize loudspeakers as actuators to drive a control signal, which adds phase to the control system. The introduction of speaker dynamics necessitates the need for further phase compensation. Several methods have been proposed to compensate for the strongly coupled dynamics of the controlled system [2, 21]. Typically these techniques apply a band-limited volume-velocity source, which are used to demonstrate dissipative feedback control. The drawback of this method is it limits performance due to the finite bandwidth

of the compensating loudspeaker. Another possibility is to use an all-pass phase correction filter in congruence with a resonant filter [3].

Research using resonant filters to control acoustic plants is limited, but has been shown to work well. The inherent limitations of these methods is the inability to perfectly collocate the sensor/actuator pair, thus allowing loudspeaker dynamics to diminish performance and stability. One report presented a procedure where the low-frequency modes of the plant were ignored, effectively allowing the phase induced by the speaker not to destabilize and erode performance on the controller [10]. Another report demonstrated a pacifying control system that utilized a feed through term for non-collocated control. However, global control was not addressed due to the sensor and error location being the same [27]. By using an all-pass filter design scheme in conjunction with PPF, global control is permitted at any sensor location. This compensation method eases the collocation requirement on the sensor/actuator pair, giving greater tolerance to the type and location of control transducer used.

Many variations of PPF can be achieved given the inherent forgiveness of high-frequency finite actuator dynamics [9]. However, structural PPF uses piezoelectric actuators which do not contribute phase, in contrast acoustic PPF utilize loudspeakers that do add phase to the system. Resonant band-pass filters, rather than low-pass filters, would be desirable when considering multi-modal control of acoustic systems. The roll-off associated with band-pass filters would limit interactions between adjacent modes. As long as the phase of the control path is compensated to the desired 180^o at each mode, stability margins can be maintained. Thus, the gain is precisely focused around the targeted resonant frequency of system.

By examining the compensating filter parameters, the control system could be optimized. As with Helmholz resonator design, if damping is high in the PPF filter, a wider band of control is created. Also, the filter gain plays an important role in controller performance. To illustrate this point a single degree of freedom system is again considered. Uncontrolled and two cases of controlled systems responses are shown in Figure 3. The first controlled system (dashed line) shows the case where either excessive gain or insufficient damping has been applied to the compensator, effectively splitting the mode [5]. The second controlled system (dash-dot line) shows the response with correct gain and damping values applied to the controller. A method has been developed to optimize damping levels, based on the

knowledge of the dc-gain and pole-zero spacing [23]. This work showed that a phase shift of 10 degrees in the control path can deteriorate control performance by as much as 70 percent.

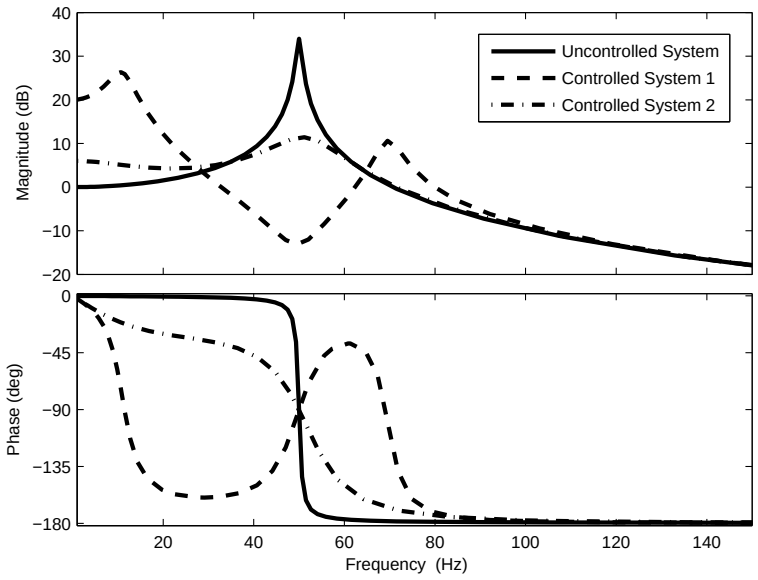

Figure 3: Uncontrolled and controlled frequency response of PPF control.

This study extends the achievements of using electronically realized Helmholtz resonators in a PPF control scheme [3]. The use of resonant filters is further investigated, by examining them in higher order models. Various types of filters are also explored (i.e. Butterworth, Chebyshev, and elliptical) and used in congruence with all-pass filter compensation arrangements. By using higher order and band-pass filters, multi-modal control becomes greatly improved due to the embedded characteristics of the filters. Finally, an adaptive gain algorithm is examined to achieve an optimized broadband multi-modal controller. Realizing the controller electronically greatly facilitates the optimization process.

2.0 THEORETICAL DEVELOPMENT

2.1 ANALYTICAL DUCT MODEL

To examine the proposed feedback ANC scheme, a one-dimensional waveguide is considered. An acoustic enclosure produces a reverberant sound field that has sparse modal shaping, allowing for close examination of the first few modes. A schematic of the enclosure can be seen in Figure 4. The dimensions of the duct are comprised of the length l_d, width w_d, and height h_d. The rigid-walled duct contains two midrange loudspeakers with a face width w_s, located at each end. One is centered at x_1 and the other about x_2, providing the disturbance and control inputs, respectively. Two acoustic sensors will provide the output signals, located at x_{perf} and x_2, which will be discussed later in Section 3.1.

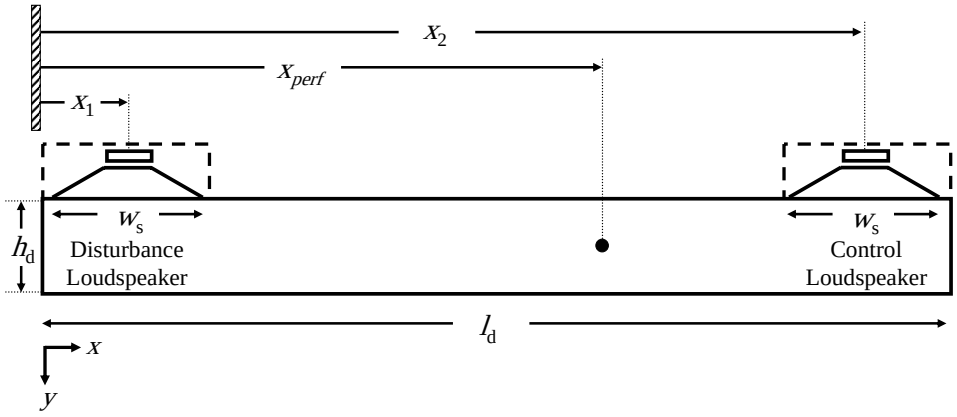

Figure 4: Acoustic duct setup.

2.1.1 Acoustic Enclosure

The pressure of the wave equation is used to model the enclosure as:

$$\nabla^2 p(x,t) - \frac{1}{c^2}\frac{\partial^2 p(x,t)}{\partial t^2} = \rho_o \sum_{j=1}^{J} \frac{\partial^2 y_j(t)}{\partial t^2}, \; n = 1 \ldots \infty, \tag{2.1}$$

where $p(x,t)$ is acoustic pressure at a distance, x, and time, t, inside the duct. The speed of sound, c, and density, ρ_o, are constant properties in air. The displacement function, $y_j(t)$, of the j^{th} speaker, is approximated as a piston. The pressure distribution of the acoustic duct in modal coordinates is expressed as a function of space and time as:

$$p(x,t) = \sum_{n=1}^{\infty} p_n(t)\Psi_n(x). \tag{2.2}$$

Where the n^{th} pressure mode and eigenfunction of the duct are given as p_n and ψ_n, respectively. By applying the proper boundary conditions the mode shapes, ψ_n, can be expressed as:

$$\Psi_n = \frac{2}{l_d}\cos\left(\frac{n\pi x}{l_d}\right). \tag{2.3}$$

By substituting Equation 2.2 into Equation 2.1 and applying orthogonality, the 2^{nd} order forced wave equation can be expressed in modal coordinates as:

$$\ddot{p_n} + 2\zeta_d\omega_n\dot{p_n} + \omega_n^2 p_n = \frac{2\rho_o c^2 A}{l_d}\sum_{j=1}^{2} \ddot{y_j}\phi_j, \tag{2.4}$$

where the duct's natural frequencies are described by:

$$\omega_n = \frac{n\pi c}{l_d}. \tag{2.5}$$

Here, the duct damping ratio, ζ_d, has been introduced to properly bound the model and represent internal dissipation. The area of the loudspeaker, A, is approximated as square to simplify calculations. The resulting modal participation function is denoted as:

$$\phi_j = \frac{2\mathrm{w}_s}{n\pi A}\left[\sin\left(\frac{n\pi x_{j2}}{l_d}\right) - \sin\left(\frac{n\pi x_{j1}}{l_d}\right)\right], \; n = 1 \ldots N, \; j = 1, 2, \tag{2.6}$$

where x_{j1} and x_{j2} denote the left and right edges of the disturbance ($j = 1$) and control ($j = 2$) loudspeaker, respectively. Also, the infinite summation over n in Equation 2.6 must be truncated at a point N that will allow the model to converge. The value of N, over the bandwidth of interest, can be determined by assuming the one-dimensional model is accurate up to the calculated lowest cutoff frequency which is computed using:

$$f_{co} = \frac{c}{2\mathrm{w}_d} = \frac{343}{0.3302\,s} = 1,039Hz. \tag{2.7}$$

The set of uncoupled equations represented in Equation 2.4 characterizes the behavior of the duct.

2.1.2 Acoustic Actuator

The actuators used to excite the acoustic system are two midrange loudspeaker that drive both the disturbance and control signals, as mentioned above. Each speaker has two inputs: pressure displacement and voltage to the coil, and one output: acceleration of the speaker cone. The loudspeakers are coupled electro-mechanical systems, thus requiring two differential equations to describe their motion. The equation of motion for the mechanical components of the loudspeakers is:

$$\ddot{y_j} + \frac{b}{m}\dot{y_j} + \frac{k}{m}y_j = \frac{Bl}{m}\,I_j - \frac{A}{m}\,p(x_j, t), \tag{2.8}$$

where m, A, b, an k, are the mass, cross sectional area, damping, and stiffness of the loudspeaker, respectively. The Bl term is the product of the magnetic flux density and the length of the coil. The electrical equation is established using Kirchoff's voltage law to produce:

$$\dot{I_j} + \frac{R_s}{L_s}I_j = \frac{v_j(t)}{L_s} - \frac{Bl}{L_s}\dot{y_j},\ j = 1, 2, \tag{2.9}$$

where L_s and R_s represent the inductance and resistance of the loudspeaker, with an input voltage $v_j(t)$. The Bl term in this equation relates coil velocity to back electro-motive force

(EMF). The above equations are used to produce a coupled acousto/mechanical equation [3], written in modal form as:

$$\ddot{y}_j + \frac{b}{m}\dot{y}_j + \frac{k}{m}y_j = \frac{Bl}{m}\,I_j - \frac{A}{m}\sum_{n=1}^{N} p_n(t)\phi_j,\ \ j = 1, 2. \tag{2.10}$$

2.2 UNCONTROLLED SYSTEM

All system components are assembled and simulated in Matlab, using state-space representation [4]. The internal dimensions of the acoustic duct and parameters of the Pearless 832592 loudspeakers used in simulations are consistent with those of the experimental test bed, which will be discussed later in Chapter 4. The acoustic sensors are Model $130D20$ microphones by PCB Piezotronics. The properties of the enclosure, mid-range loudspeakers, and air can be seen in Table 1. All experimental data was obtained using a SigLab Model $20-40$ spectrum analyzer.

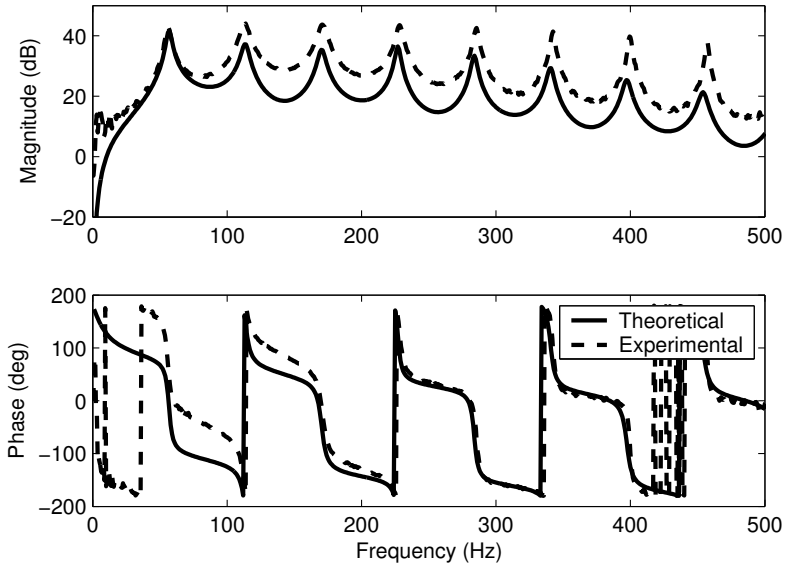

Figure 5: Simulated and experimental results for uncontrolled system.

Table 1: Plant parameters used in simulation.

Duct		*Loudspeaker*	
Param.	Value	Param.	Value
l_d	$3.0\,m$	A	$85.0\,cm^2$
w_d	$16.5\,cm$	b	$1.30\,Ns/m$
h_d	$16.5\,cm$	k	$12.5\,kN/m$
w_s	$9.22\,cm$	m	$7.8\,g$
x_1	$0.1\,m$	Bl	$5.5\,N/A$
x_2	$2.9\,m$	L_s	$1.1\,mH$
ρ_o	$1.23\,kg/m^3$	R_s	$6.1\,\Omega$
c	$346\,m/s$	-	-

To verify the model, the analytical frequency response between $v_1(t)$ and $p(x_{perf}, t)$ is plotted against measured results from the duct as shown in Figure 5. This response consists of the disturbance speaker and duct, measured at $p(x_{perf}, t)$ set equal to x_2. This path will be referred to as the disturbance/performance path, which will be expanded upon later in Section 3.1. Note that the rigid walled duct theoretically has an infinite number of modes. However, the low-frequency model from $0 - 500\,Hz$ is found to converge at $N \geq 36$, thus $N = 40$ is selected to ensure a modally rich system.

It is observed from Figure 5 that the analytical model predicts the behavior of the experimental test bed well. Negligible discrepancies between the simulated and experimental duct will not inhibit the implementation of the control system. Efforts will now be focus on developing a controller that can control any exclusive or multiple pressure mode(s) shown in Figure 5.

3.0 CONTROL SIMULATION

A compensator that will attenuate the resonant modes of the duct is developed and discussed in this chapter. The adopted control scheme is similar to PPF used for structures, but has been extended to acoustic systems [3, 29]. A collocated sensor/actuator pair produces a reference pressure that is fed back through a tuned compensating filter to produce a signal that is 180^o out of phase with the input signal at the control frequency, ω_c. Loudspeaker actuator dynamics add phase to the system, which is not observed in structural PPF examples [9, 12]. These undesired dynamics are compensated for by employing an all-pass filter in series with the magnitude-shaping filter [3, 4].

The achievements made by prior acoustic PPF studies is extended through examination of analytical simulations [29]. Previously, only modest attempts at multi-modal control have been attempted. Phase interactions between uncontrolled and controlled duct modes is examined for both single and multi-modal cases. Compensator damping determines the amount of phase interaction that will occur between modes, due to resonant filter roll-off. Different types of higher-order filters are investigated to improve controller performance. To gain greater insight into controller stability and performance, Nyquist stability is examined, as opposed to root-locus stability analysis. Realizing the control system electronically, through a digital signal processor (DSP), allows for easy implementation of higher-order filters. The DSP board also permits the multi-modal controller to use the same hardware (i.e. DSP, loudspeaker, and microphones), and facilitates the examination of compensator design variables.

In this chapter, control system modifications are simulated on the analytical duct model. The transfer function paths associated with the control system configuration are examined. A single mode controller is developed, which consists of a resonant magnitude-shaping filter and

a phase-correction filter. Effects of modifying the resonant filter damping, order, and design-type are investigated. The procedure is then extended to the design and demonstration of the a multi-modal controller.

3.1 CONTROL SYSTEM CONFIGURATION

A diagram showing the active component system interactions can be seen in Figure 6. The duct model has two acceleration inputs, $\ddot{y}_1$ and $\ddot{y}_2$, which are obtained from the disturbance and control loudspeakers, respectively. The duct component also has four pressure outputs, the first ($p(x_1, t)$) and last ($p(x_2, t)$) of which are the pressure inputs acting on the disturbance and control speakers, respectively. The second ($p(x_{perf}, t)$) and third ($p(x_{sen}, t)$) outputs of the duct model represent the performance and sensor pressure measurements, used to assess effectiveness and drive the control system.

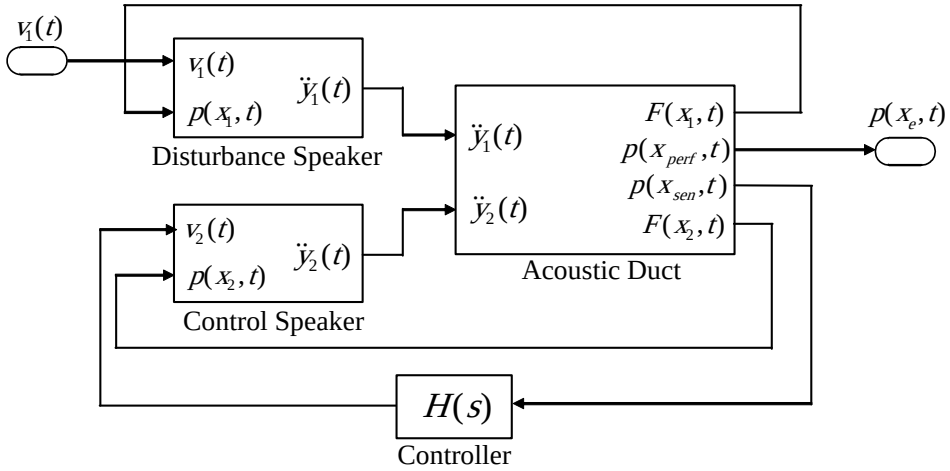

Figure 6: Schematic of system conventions.

There are four distinct transfer function paths that are associated with the control system in Figure 6. The speaker voltage signals $v_1(t)$ and $v_2(t)$ create the disturbance and control path inputs, respectively. The measured pressure signal, $p(x_{perf}, t)$ and $p(x_{sen}, t)$, form the performance and sensor path outputs, respectively, which are governed by the placement

of microphone sensors. These transfer function paths are shown in Figure 7 in a standard two-port block diagram [24]. The disturbance/sensor path, $H_{ds}(s)$, is the primary transfer function path targeted for sound level reduction. The disturbance/performance path, $H_{dp}(s)$, gives an independent measurement of controller performance, free of the sensor path measurement. The effectiveness and stability of the control system is determined by the control/sensor path, $H_{cs}(s)$, which will be discussed later in Section 3.3. Both collocated and non-collocated control, discussed in later in Section 4.1.1 and 4.1.2, have the same transfer function paths shown Figure 7.

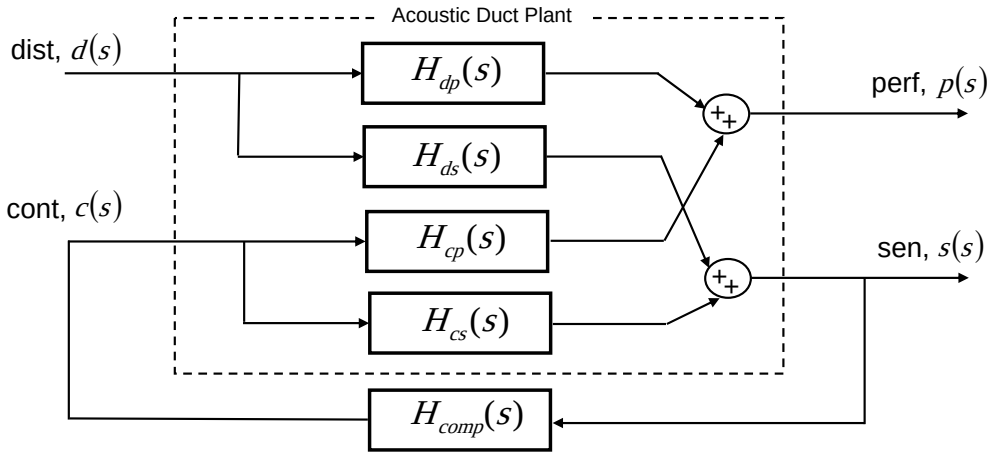

Figure 7: Transfer function paths for duct test bed.

3.2 COMPENSATOR DESIGN

As stated above, the resonant mode controller is designed using a PPF configuration [12]. The collocated sensor/acuator is used to detect a signal that, with the resonant filter, is 180^o out of phase at the chosen control frequency, ω_c. However, loudspeaker dynamics add phase to the control path, thus eroding performance and stability [3]. This is not observed in structural PPF, since the piezoelectric actuators do not contribute phase in the bandwidth of the control system. In addition to phase introduced by the acoustic actuator, the DSP

board that is used to implement the resonant filter also contributes phase to the system [29]. Thus, a digital version of the all-pass filter network is used to compensate for these phase shifts. The acoustic resonant mode controller consists of either a band-pass or low-pass filter, and a phase-correcting all-pass filter.

In this section, a compensating filter network, $H_{comp}(s)$, that will produce the control signal is designed. For a stable closed-loop feedback system, it is desired that the phase at the targeted frequency, ω_c, be $\pm 180^o$. For a the two-port system shown in Figure 7, the phase at the control frequency is found by examining the control/sensor path, $H_{cs}(s)$. The total phase at the compensator is described by:

$$\theta_c(\omega_c) = \theta_f(\omega_c) + \theta_a(\omega_c) = \theta_s(\omega_c) + \theta_d(\omega_c) + \theta_{dsp}(\omega_c). \tag{3.1}$$

The phase contribution is constant for loudspeakers, $\theta_s(\omega_c)$, duct, $\theta_d(\omega_c)$, and unit sample delay from the DSP, $\theta_{dsp}(\omega_c)$. The phase induced by the resonant filters in the controller, $\theta_f(\omega_c)$, are 90^o for low-pass filters and 0^o for band-pass filters. Thus, some form of fine-tuning phase adjustment will be required, due to phase added to the control/sensor path. This is achieved through implementing an all-pass filter [3], via the $\theta_a(\omega_c)$ term in Equation 3.1, which be discussed later in Section 3.2.2.

As stated above, in order to design the controller the transfer function path $H_{cs}(s)$ must be examined. The control/sensor path determines the performance and stability of the "closed loop" controlled system. The frequency response function (FRF) of the simulated control/sensor path, which includes speaker dynamics, is shown in Figure 8. Both the control frequency, ω_c, and the phase that occurs at the control frequency, θ_c, are determined from the control/sensor path. These two parameters govern the corner frequency of the resonant filter, and the phase that will be imposed by the all-pass filter. The design of the controller components and their impact on the control/sensor path will be discussed in the subsequent sections.

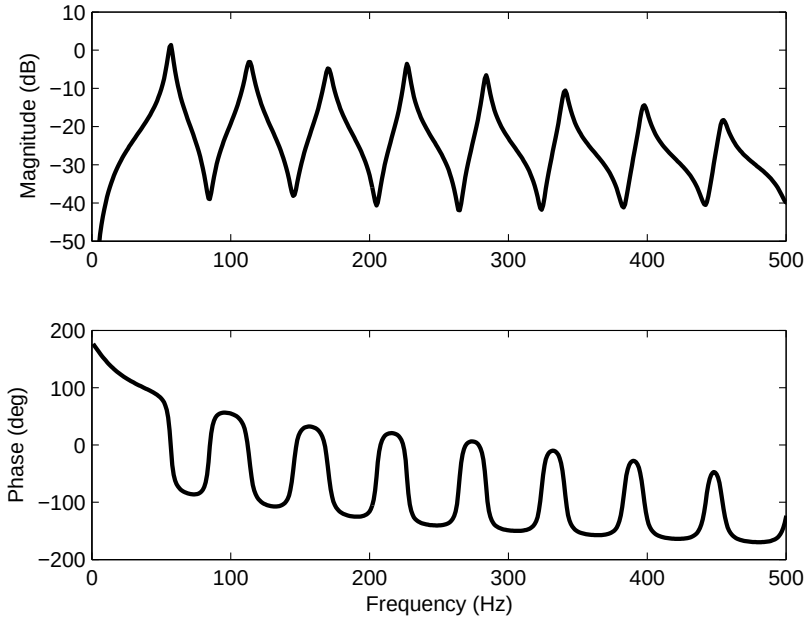

Figure 8: FRF of uncontrolled control/sensor transfer function path.

3.2.1 Resonant Compensating Filter

The resonant filter can provide gross phase compensation, and adds damping to the system. Previous studies have examined using resonant 2^{nd} order filters as the compensating filters [3, 29]. Figure 9 shows a comparison of the control/sensor path with resonant low-pass(LPF) and band-pass (BPF) filters tuned to the fundamental resonant frequency of the duct. From the right-hand Bode plot, a low-pass filter provides fast roll-off of $40\,dB/dec$ above ω_c, and yields no magnitude change to the control/sensor path below ω_c. In contrast, the band-pass filter depicted in the left-hand plot provides attenuation in the low and high frequency regions, below and above ω_c at a rate of $\pm 20\,dB/dec$.

Although low-pass filters have been shown to work well for single mode control [4], band-pass compensating filters are exclusively considered in this study. The roll-off characteristics above and below ω_c makes these filters more desirable for multi-modal control applications, by mitigating the need for an iterative control design. Unlike band-pass filters, low-pass filters cause low frequency phase interactions in controlled modes. The amount of phase

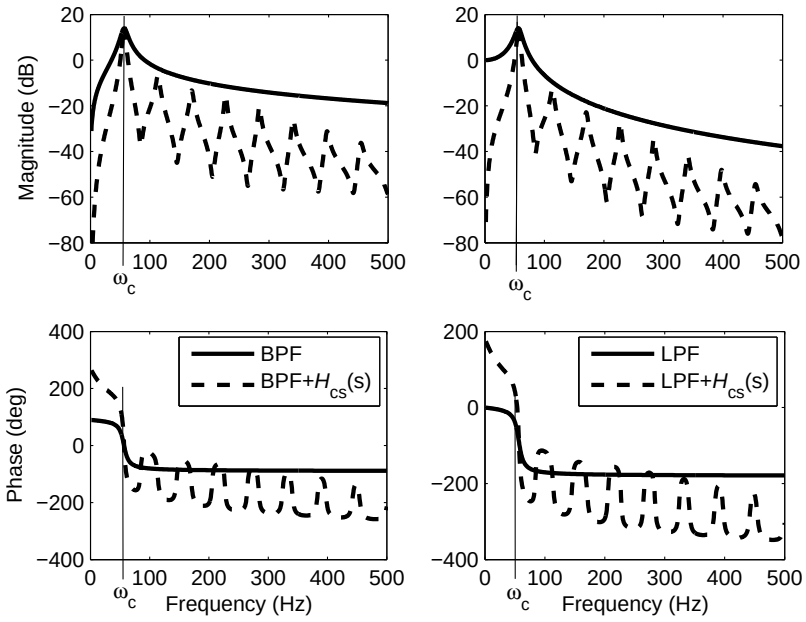

Figure 9: FRF of control/sensor path with band-pass (left) and low-pass (right) filters.

interaction is dependent on the amount of damping present in the band-pass filter, which has both high and low frequency attenuation. The transfer function of the band-pass filter is given as:

$$H_{BPF}(s) = \frac{\pm K(\frac{\omega_c}{Q})s}{s^2 + (\frac{\omega_c}{Q}) + \omega_c^2}, \tag{3.2}$$

where

$$Q = \frac{\omega_c}{BW} = \frac{\omega_c}{\omega_2 - \omega_1} \simeq \frac{1}{2\zeta}. \tag{3.3}$$

The variables Q and K represent the quality factor and gain, respectively. These quantities take into account both the speaker amplifier and microphone dynamics. The filter bandwidth (BW) is determined by the filter corner frequencies, ω_2 and ω_1, which establishes filter damping [31]. Note that the quality factor, Q, used to design the filter is inversely proportional to the damping ratio.

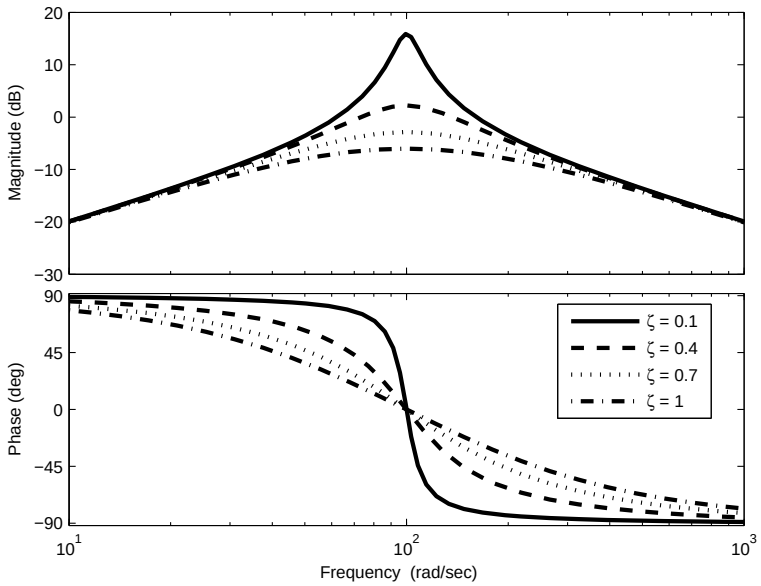

Figure 10: Frequency response of 2^{nd}-order band-pass resonant filter.

Filter damping determines the how sharply the filter rolls off, as well as the amount of control to be expected [5]. This is illustrated using a 2^{nd}-order band-pass filter with a varied damping ratio shown in Figure 10. As the damping is increased the filter poles move away from the imaginary axis, giving more control and higher gain margins. However, this comes at a cost of roll-off which causes larger regions of phase shift. Gradual phase shift can lead to unwanted phase interactions between modes (i.e. spillover) [29]. Due to their low order, resonant filters are found not to provide adequate roll-off for multi-modal control applications.

In addition to 2^{nd} order resonant filters, higher-order digital band-pass filters are also investigated for single and multi-modal control applications. They were found to be better numerically conditioned, and thus provide a more stable "open loop" compensator. There are 3 types of digital filters that are readily available: Butterworth, Chebyshev, and Elliptical. A comparison of these different types of 4^{th}-order filters tuned to $56.6\,Hz$ of the control/sensor path is considered in Figure 11. Using the observations made above in Figure 10, filter damping in Equation 3.3 is chosen heuristically. However, if there is too much damping present, phase interaction will occur due to the gradual phase shift (Figure 10). If sparse

filter damping is present, then the bandwidth becomes too small to achieve any appreciable control [8]. Both Chebyshev (dashed line) and Elliptical (dash-dot line) filters shown in Figure 11 have fast roll-off rates at the cost of ripple in the pass-band that is undesirable. Pass-band ripple relaxes damping in the filter pass-band, between ω_1 and ω_2 in Equation 3.2, which leads to poor control. However, Elliptical filter design allows for increased stop-band attenuation. The Butterworth filter (solid line) has a flat pass-band and a moderate roll-off of $\pm 40\, dB/dec$.

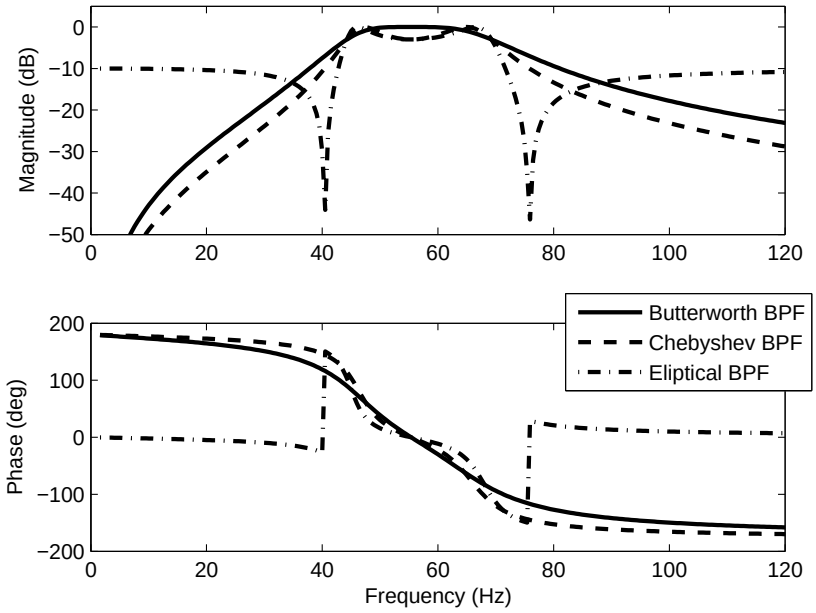

Figure 11: Comparison of 4^{th}-order digital filters for first mode control.

Either a Butterworth, Chebyshev, or Elliptical band-pass filter will be used for the resonant magnitude-shaping filter in the controller. The contrasting filter designs are preformed continuous time domain, using the appropriate design algorithm to calculate pole/zero locations [31, 22]. Higher-order filters are designed in 2^{nd}-order segments and combined together. Thus, the order of the resonant filter must always be an even integer. The effects of using higher-order filters is evaluated during control simulation in Sections 3.3 and 3.4. Butterworth, Chebyshev, and Elliptical band-pass filters are designed ranging from 2^{nd} to 8^{th} order. Altering these parameters dose not change the 0^o of phase added to the control/senosr path

by the band-pass filter at ω_c, and compensator design for remains unchanged for single mode control. However, all parallel connected band-pass filters must be taken into account when designing a multi-modal controller due to phase interactions above and below ω_c. Whether attempting single or multiple mode control, the phase induced by the loudspeaker and DSP still need to be accounted for in order to achieve the control signal.

3.2.2 Phase Compensation

Although the single-mode, band-pass compensating filter contributes no phase to the control/sensor path, the phase introduced by the loudspeaker needs to be accounted for [3]. In order to achieve a control signal that is perfectly out of phase, an all-pass phase correction filter is employed [4]. The all-pass filter has no adverse impacts on the magnitude of the control paths. Thus, the achievements made by the band-pass filter are not effected. However, when attempting multi-modal control phase shifts are introduced by the parallel connection of the resonant filters. The phase induced by multi-modal control can still be accounted for with the use of the all-pass filter phase correction scheme, due to the damping added to the compensator by the band-pass filter.

An all-pass filter can provide a non-inverting phase shift ranging from $0^o - 180^o$, and an inverting phase shift of $180^o - 360^o$. The phase shift required of the all-pass filter is dependent upon the phase present at the control path targeted frequency. The Laplace transfer function of the all-pass filter is expressed as:

$$H_{AP}(s) = \frac{\pm(s-z)}{s+p}, \tag{3.4}$$

where, z and p are the locations of the all-pass filter zero and pole, respectively. The phase angle required of the all-pass filter is determined by rearranging Equation 3.1 as:

$$\theta_a = 180 - \theta_c(\omega_c) = \theta_f(\omega_c) + \theta_s(\omega_c) + \theta_d(\omega_c) + \theta_{dsp}(\omega_c). \tag{3.5}$$

The phase at the control frequency in Equation 3.5 is subtracted by 180^o to find the all-pass filter phase contribution . Note that $\theta_c(\omega_c)$ could be any angle between 0^o and 360^o, and the

phase contribution for all other system components is constant. Thus, both inverting and non-inverting all-pass filter pole/zero locations are determined by:

$$p = z = \begin{cases} \frac{\omega_c}{cot(\frac{\pi\theta_a}{360})} & \text{if } 0^o < \theta_a \leq 180^o, \\ -\frac{\omega_c}{tan(\frac{\pi\theta_a}{360})} & \text{if } 180^o < \theta_a \leq 360^o. \end{cases} \tag{3.6}$$

The all-pass filter is created using the pole/zero found in Equation 3.6 and substituted into the transfer function in Equation 3.4. Once the all-pass filter is designed, it is combined in series connection with the magnitude shaping filter described in Section 3.2.1. The compensator (BPF + APF) will produce a signal that is 180^o out of phase at ω_c on the control/sensor path.

3.3 SINGLE MODE CONTROL

A control system that can control any single mode, will be demonstrated on the analytical duct model. The controller consists of a band-pass filter and a phase-compensating all-pass filter. The control frequency, ω_c, along with the control phase angle, θ_c, are chosen from the uncontrolled control/sensor path in Figure 8. Equation 3.5 is then used to calculate the phase required of the all-pass filter. Both disturbance paths, $H_{dp}(s)$ and $H_{ds}(s)$ in Figure 8, will be used to evaluate the performance of the controller. Control of a single duct mode will first be considered here, and the procedure will be extended to the multi-modal case in the next section.

A single mode controller is developed using the components described in Sections 3.2.1 and 3.2.2. The first pressure node of $56.6\,Hz$ is targeted for control. In examining Figure 8, it is realized that $\theta_c(\omega_c) = 4^o$ for the fundamental duct mode. Thus, from Equation 3.5, the all-pass filter must provide a non-inverting phase angle of 176^o. The single-mode compensator consists of a resonant magnitude-shaping filter with a band-width of $30\,Hz$, tuned to the first mode, placed in series with an all-pass filter.

As stated above, the stability and performance of the system is determined by the control/sensor path. In order to establish the gain to be applied to the compensator, standard

Nyquist Stability criterion is examined. Lyapunov stability analysis [9] is inappropriate since a non-minimum phase plant dose not exist for acoustic plants. A Nyquist plot of the controlled H_{cs} transfer function path with unity gain, without (dashed) and with (solid) all-pass filter phase compensation, can be seen in Figure 12. The controller consists of a 4^{th}-order Butterworth band-pass filter and all-pass filter. The gain margin for the phase-compensated system is $16.6\,dB$, while the gain margin for the system with just band-pass filter compensation is $-1.48\,dB$ (unstable). Although the system isn't unconditionally stable, the addition of the all-pass filter rotates the targeted (largest) loops away from the -1 point, improving the gain margin. Note from Figure 12 that the uncontrolled modes are de-emphasized by the band-pass filter (located around the origin) and thus have a much higher gain margin than the targeted mode. The same analysis is used for Chebyshev and Elliptical type band-pass filter compensators to achieve similar results.

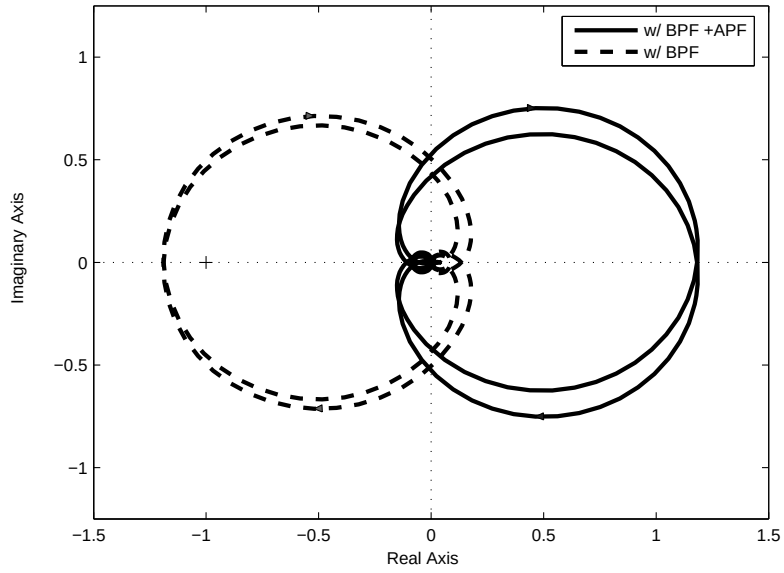

Figure 12: Nyquist plot of control/sensor path with and without phase compensation.

In order to find an optimal controller, the resonant filters discussed in Section 3.2.1 are compared in control simulations. The best performing controller will achieve a reduction in the targeted mode while also attenuating signal energy. Thus, a compensator that produces

spill-over due to adjacent mode phase interactions will be observed as poor control. Using signal energy as a measure of control system performance allows for adaptation of system parameters, discussed in Chapter 5. Each controller is designed as described above, but the type and order of the resonant filter is varied. Compensator damping is chosen heuristically, which remains the same for all cases. A different gain is used for each case, by dividing the gain margin in half. However, this guarantees that the stability is the same for all compensator designs.

The effects of varying both the order and design type of the band-pass filter is examined. A comparison of different order Chebyshev filters on the disturbance/sensor path is shown in Figure 13. Although the 2^{nd}-order filter achieves the best reduction, poor roll-off allows for unfavorable phase interactions in the 2^{nd} mode (spill-over). A similar comparison is done for Butterworth and Elliptic filters, and it is found that 4^{th}-order filters (dotted line in Figure 13) perform the best for all filter design types, due to targeted mode reduction and unchanged performance in the next adjacent mode. A control simulation comparison of 4^{th}-order Butterworth (dashed), Chebyshev (dotted), and Elliptical (dash-dotted) compensators on the disturbance/sensor path is shown Figure 14. The Chebyshev compensator only achieves a reduction of $6\,dB$, due to the pass-band ripple explained in Section 3.2.1. The elliptic filter gives a reduction $8\,dB$ and appears to have reduced the response at higher modes, due to favorable phase interactions (100^o or more of phase added at the uncontrolled resonant frequencies) . However, this result is not observed on the experimental test bed, which will be discussed in Chapter 4. The Butterworth compensator provides best attenuation of $10.5\,dB$, with very little spill-over in the next mode.

Single mode control can be extended to any desired mode providing modal spacing is sufficient [8]. A 4^{th}-order Butterworth band-pass filter is used to design a compensator to individually control the first three analytic duct modes. Figure 15 shows the simulated magnitude response of the disturbance/sensor path of single mode control on each of the first 3 modes. A reduction of $8\,dB$ is now seen on the 2^{nd} and 3^{rd} modes respectively, showing that any single duct mode can be targeted and attenuated. Efforts are now directed at developing a compensator to control more than two modes.

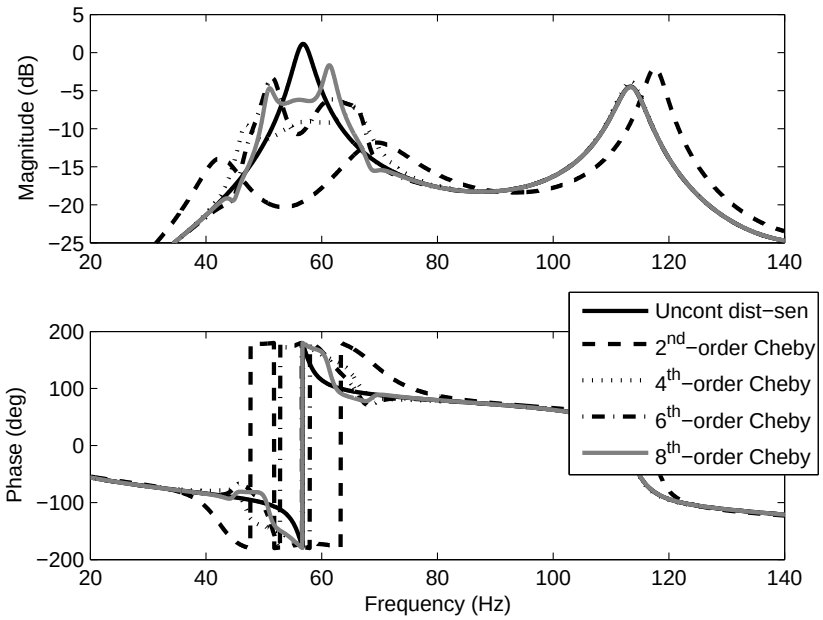

Figure 13: Comparison of different order Chebyshev controller responses.

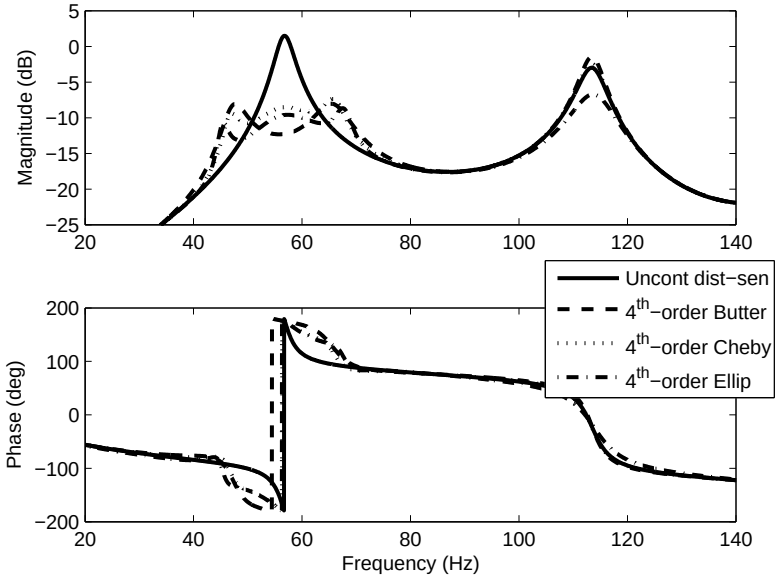

Figure 14: Simulated control comparison with 4^{th}-order control filters.

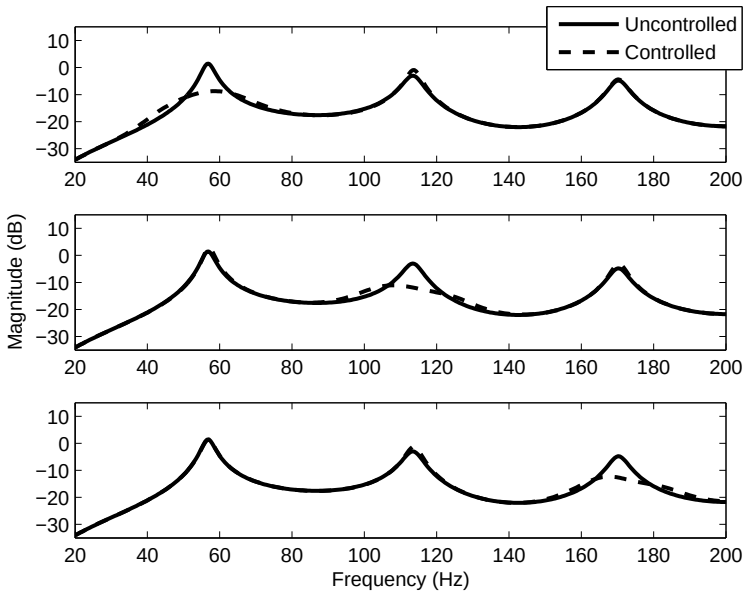

Figure 15: Magnitude response of the disturbance/sensor path for 3 single-mode controls.

3.4 MULTIPLE MODE CONTROL

The procedure for controlling a single acoustic mode is now extended to controlling multiple modes. Returning to Figure 8, the first 4 pressure modes are targeted for control. The compensator is realized in the same manner as the single mode case. The phase of the control/sensor path shown in Figure 8 is examined with the addition of the 4^{th} order Butterworth band-pass filters. Equation 3.1 is used to find the phase for each mode at the control frequency that is desired for control. An iterative design approach is adopted, and all-pass filters are implemented at each mode to achieve the desired 180^o of phase at each mode. The same stability analysis that was performed on the single mode controller is used here. This design process is repeated for all higher-order filter designs, as done in the single-mode case. Each mode controller, which consists of a compensating filter and phase correction filter, is connected in parallel to form the multi-modal controller.

Using Higher-order band-pass filters for multi-modal control decouples adjacent modes from control. As an example, 4^{th}-order Butterworth band-pass filters(solid line) and their impact on the first 4 modes of the analytic duct (dashed line) can be seen in Figure 16. Filter

bandwidth, and therefore damping, is chosen heuristically. The band-pass filter's relatively sharp phase shift at the control frequency, caused by the addition of higher order poles, limits phase interaction and decouples adjacent modes from control. Using these higher-order band-pass filters ensure better performance in the pass-band and roll-off regions. The same decoupling effect can be demonstrated for both Elliptical and Chebyshev filters.

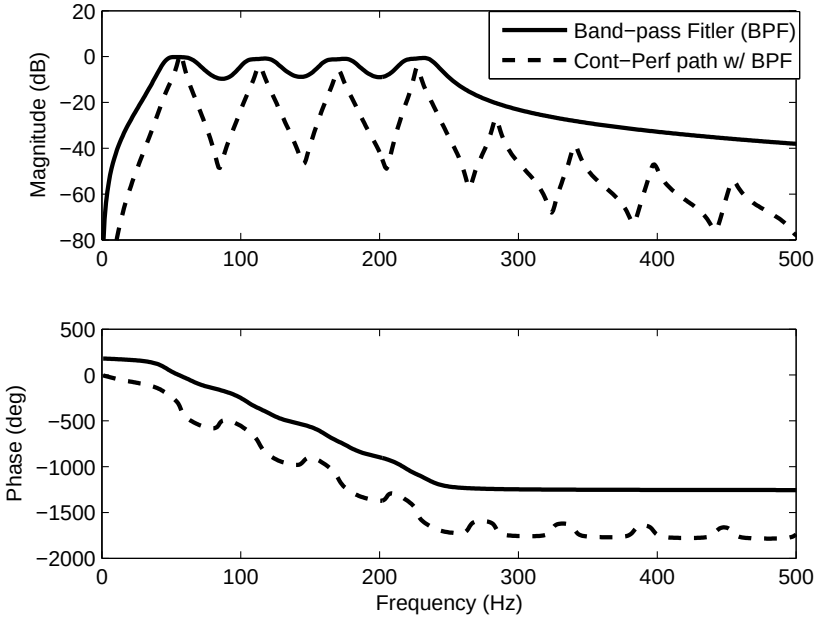

Figure 16: FRF of 4^{th}-order band-pass filters on the simulated control/sensor path.

A comparison of different types of higher-order multi-modal compensators is done in same manner as shown in Section 3.3. Each compensator uses either a Butterworth, Chebyshev, or Elliptic filter and is designed to attenuate the first 4 pressure modes of the analytical duct. The same iterative design for the all-pass filter is adopted for all compensator types. Damping for each parallel compensator is chosen heuristically, but is the same for all cases. Stability also remains the same by using different gains based on half the gain margin for each compensator design. Again, the best performing compensator achieves reductions at the targeted mode while also attenuating total signal energy. A comparison of different order Elliptic controllers can be in seen in Figure 17, which shows that the 6^{th}-order filter (dash-dot) achieves the best control (due to spill-over observations). Similar comparisons are done to find the 4^{th}-order Butterworth and Chebyshev filters perform the best. Next, a

comparison of a 4^{th}-order Butterworth filter, 4^{th}-order Chebyshev filter, and 6^{th}-order Elliptic filter controllers is performed on the disturbance/senosr path in Figure 18. The Chebyshev (dotted) and Elliptical (dash-dot) compensators display an adequate control with an average reduction $7\,dB$ and $8\,dB$, respectively. However, the Butterworth compensator achieves the best average reduction of $9\,dB$.

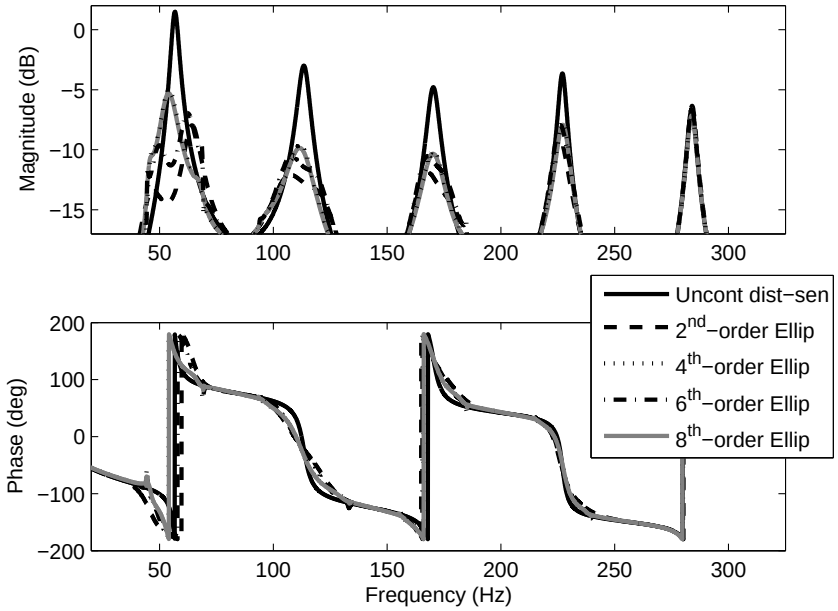

Figure 17: Simulated comparison of different order Elliptic compensator responses.

The simulation of multi-modal control on the first 4 modes of the analytic duct be seen in Figure 19. An average attenuation of $9\,dB$ is observed in the targeted modes on the disturbance/performance path with little spill-over ($1\,dB$ in the 5^{th} mode). Note that no optimization was performed on the compensator(s) to ensure more desirable results for the simulations. Improvements are expected if individually tailored gains and damping levels are considered for each modal compensator, which is addressed in Chapters 4 and 5.

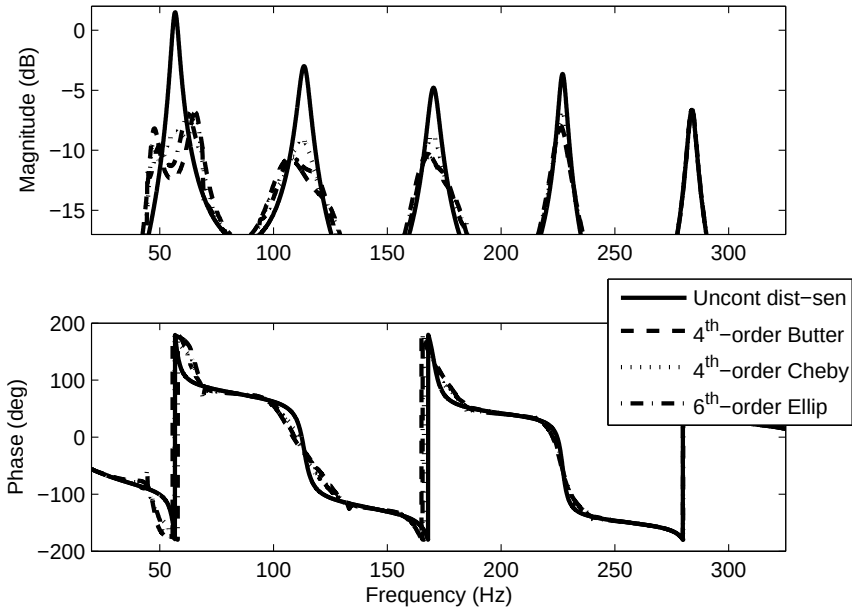

Figure 18: Simulated comparison of multi-modal Butterworth, Chebyshev, and Ellipitical controller responses.

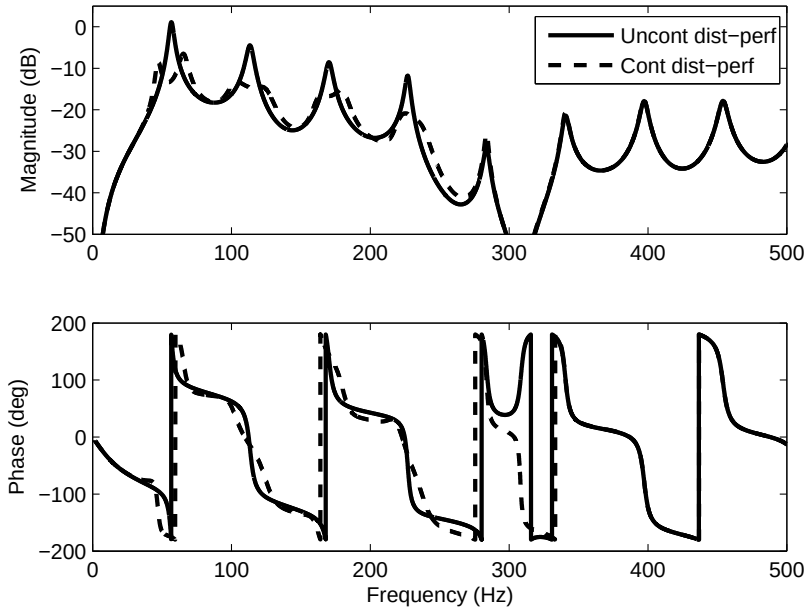

Figure 19: FRF of simulated disturbance/performance path showing 4-mode control.

4.0 EXPERIMENTAL DEMONSTRATION

The resonant mode controller is demonstrated on rigid walled acoustic duct shown in Figure 20. The experimental test bed is constructed with $1.9\,cm$ thick plywood, and is sealed with silicone caulking. The internal dimensions are consistent with analytical model, given in Table 1. The identical Peerless model 832592 loudspeakers are mounted in sealed boxes with internal volume of $2,304\,cm^3$. Nine sealable ports, $\Delta x = 0.1\,m$ apart, located along the top edge of the duct are used for sensor and error measurements. The tenth port is used for the primary sensor location as shown in Figure 5. A schematic showing sealable measurement ports of the acoustic duct can be seen in Figure 21. The input to the disturbance speaker is a white noise signal with a bandwidth of $1000\,Hz$, generated with a SigLab Model $20-40$ spectrum analyzer. The controller was initially implemented on a $TMS320C30$ based DSP board [29], but later using the Matlab real time interface with a DSpace$^{\text{TM}}$ 1104 R&D controller board.

The acoustic duct is chosen as the test bed to be controlled because of its sparse modal spacing. The acoustically excited enclosure allows for close examination of the first few low-frequency modes. However, it is expected that systems with medium to high modal density could also be controlled. Recall that the resonant mode controller is modeled after a passive Helmholtz resonator, which can work at middle to high frequencies. The passive Helmholtz resonator is inherently stable and its performance is governed by the amount of passive gain created by the combination of the plant and resonator. The proposed resonant mode controller is expected to perform (as a notch filter) in these cases, as long as the gain is low enough that Bode stability is maintained [13].

Results shown during simulations are now demonstrated on the experimental test bed. The same design procedure that was used during control simulations is used here to develop

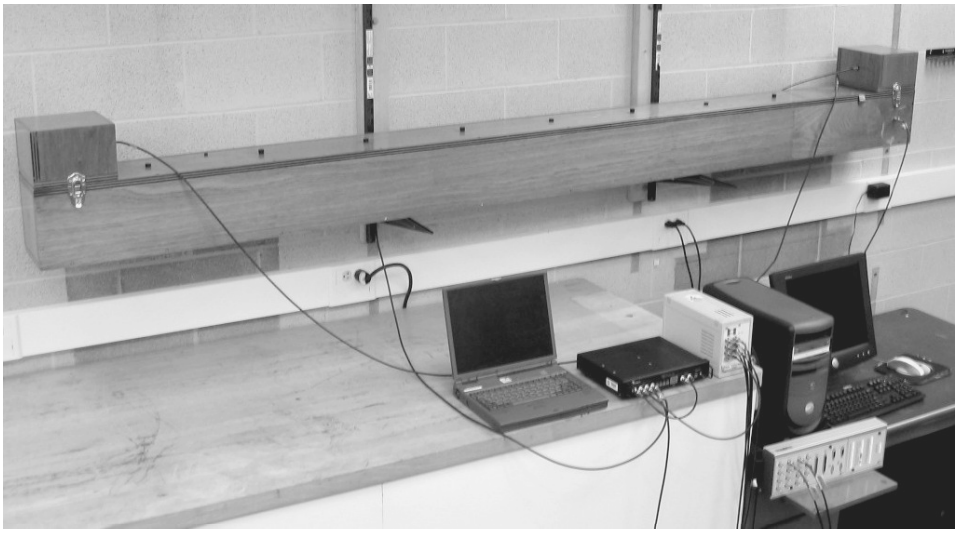

Figure 20: Picture of the experimental acoustic duct.

the experimental resonant mode compensator. First, a single mode controller is developed to attenuate the response at the first duct pressure node. Both collocated and non-collocated single mode control will be examined. The controller design is then extended to multi-modal control of the first 4 duct modes. Global control is investigated and demonstrated by examining the measurement ports along the duct axis for both single and multi-modal control.

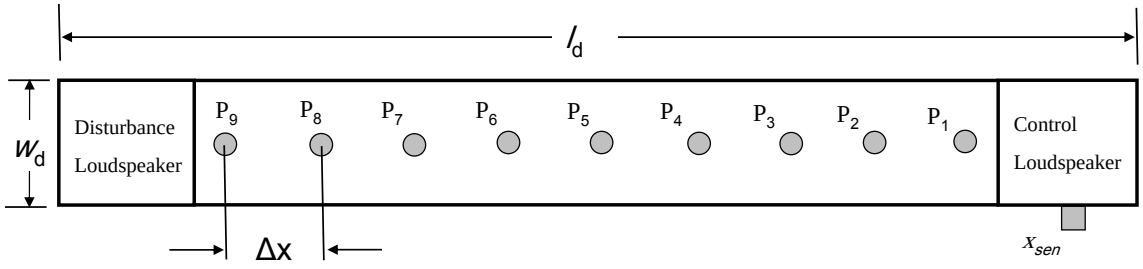

Figure 21: Measurement ports along the acoustic duct.

4.1 SINGLE MODE CONTROL

The resonant mode controller is now demonstrated on the experimental test bed to control the first acoustic mode. The same design procedure that was used to develop the single mode controller during simulation is used here. The two-port diagram shown in Figure 7 used to define the transfer function paths during simulations is used to describe the transfer function paths of the experimental duct. The uncontrolled control/sensor path, $H_{cs}(s)$, is examined to determine the phase at the control frequency. Next, a Butterworth band-pass filter is added to $H_{cs}(s)$, tuned to the desired mode of control. A phase-compensating all-pass filter is then added to the controller to ensure that a 180^o phase shift occurs at ω_c. The effectiveness of the controller is evaluated on the disturbance paths, $H_{ds}(s)$ and $H_{dp}(s)$. It was shown during control simulations in Chapter 3 that any single mode can be controlled, which is also the case here. Also, the Nyquist stability analysis that was illustrated during single mode simulation is applied here in the experimental demonstration.

All ANC systems use a loudspeaker as an actuator to drive a control signal. The control speaker effectively adds energy to the system, which could conceivably be preventing the disturbance speaker from actuating (i.e. source-loading). However, unlike feedforward methods where energy densities and an *a priori* reference signal must be considered [26], feedback control can augment the system parameters to ensure that the disturbance speaker is uninhibited. By measuring the surface acceleration and power input to the disturbance speaker, which remained unchanged for both uncontrolled and controlled cases, a non-source loaded compensator was confirmed. This was achieved using a model $U352C22$ accelerometer by PCB Piezotronics and a post processing integrator circuit. The results comparing disturbance speaker power, acceleration, and velocity for uncontrolled and controlled cases can be seen in Table 2.

Reducing the noise at a specific location often has the unwanted side effect of increasing noise elsewhere. However, the rigid-walled duct creates a simple sound field that makes global reduction possible. Unlike other works [16, 27], the performance sensor can be moved along the 10 equally space ports along the duct axis, shown in Figure 21, to evaluate whether or not global control is achieved. Two types of control will be considered for single mode

Table 2: Source loading measurements.

Measurement	Uncontrolled	Controlled	Difference
Acceleration	$0.7822\,V_{rms}$	$0.7891\,V_{rms}$	0.8783%
Velocity	$0.6390\,V_{rms}$	$0.6443\,V_{rms}$	0.8260%
Power	$0.0988\,W_{rms}$	$0.0976\,W_{rms}$	1.2220%

control, collocated and non-collocated. Collocated control places the sensor microphone, x_{sen}, directly under the control loudspeaker. Non-collocated control places the x_{sen} at one of the nine equally spaced measurement ports ($P_1 - P_9$ in Figure 21) along the duct axis. Both cases still form the transfer function paths shown in Figure 7, and the same design procedures must be followed. Also, note that both case still use the performance microphone, x_{perf}, to assess global control and compensator effectiveness. Although more complicated, the same results can be shown for multi-modal control.

4.1.1 Collocated Control

For this case of single mode control the sensor microphone, x_{sen}, is collocated with the control actuator. In order to develop the experimental controller, the control/sensor path must be examined. The duct is excited via the control loudspeaker with a $1000\,Hz$ white noise signal. The sensor microphone is used to detect the disturbance signal that will be fed through the DSP board. The experimental uncontrolled control/sensor path, which contains phase contributions from both the speaker dynamics and DSP card, is shown in Figure 22.

The first duct mode on the experimental test bed of $54.37\,Hz$ is targeted for reduction. The same design processes used during control simulations is used here to develop the compensator, which consists of a magnitude-shaping band-pass filter in series with an all-pass filter. The phase at the first mode resonant frequency, $\theta_a(\omega_c)$ is found by examining Figure 22. The phase required of the all-pass filter is found by using Equation 3.4, and the pole/zero locations are found by using Equation 3.6.

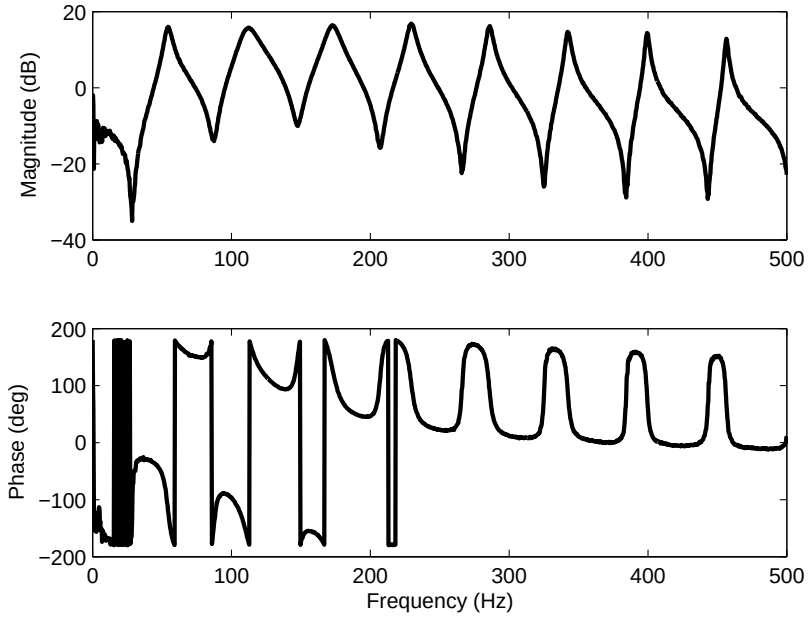

Figure 22: FRF of the experimental control/sensor path.

The resonant filter comparison that was shown in Section 3.3 is now extended to the experimental system. The compensator damping is again chosen heuristically, but is the same for all cases. However, for this comparison the same gain is applied to all compensators. Each compensator is descretized by utilizing a Tustin approximation with frequency prewarping at ω_c. The highest allowable sampling rate is used for each compensator design, which is determined by the poles of the compensator. Stability of the discrete compensator is examined using z-plane stability [22]. As sampling is increased the poles of the compensator move towards the unit circle. A comparison of different order Elliptic filters on the disturbance/sensor path is shown in Figure 23. A similar comparison is done for Butterworth and Chebyshev filters, and it is found that 4^{th}-order filters (dotted line in Figure 23) perform the best for all filter design types. A control simulation comparison of 4^{th}-order Butterworth (dashed line), Chebyshev (dotted line), and Elliptical (dash-dotted line) compensators on the disturbance/sensor path is shown Figure 24. The 4^{th}-order butterworth filter obtains a $2\,dB$ better reduction than either the Chebyshev or Elliptic 4^{th}-order filters without spill-over.

The results of collocated single mode control on the first duct mode can be seen in Figure 25. The compensator consists of the same 4^{th}-order Butterworth filter and all-pass filter as designed above. However, the gain applied to the controller and damping is chosen heuristically to ensure maximum attenuation. The performance microphone is placed at the measurement port closest to the collocated sensor microphone (P_1 in Figure 21). A reduction of approximately $7\,dB$ is observed on the disturbance/performance path with no appreciable spill-over in the next adjacent mode. Less than $1\,dB$ of attenuation is noted in the 3^{rd} mode, due to a favorable 100^o or more of phase that has been introduced by the controller.

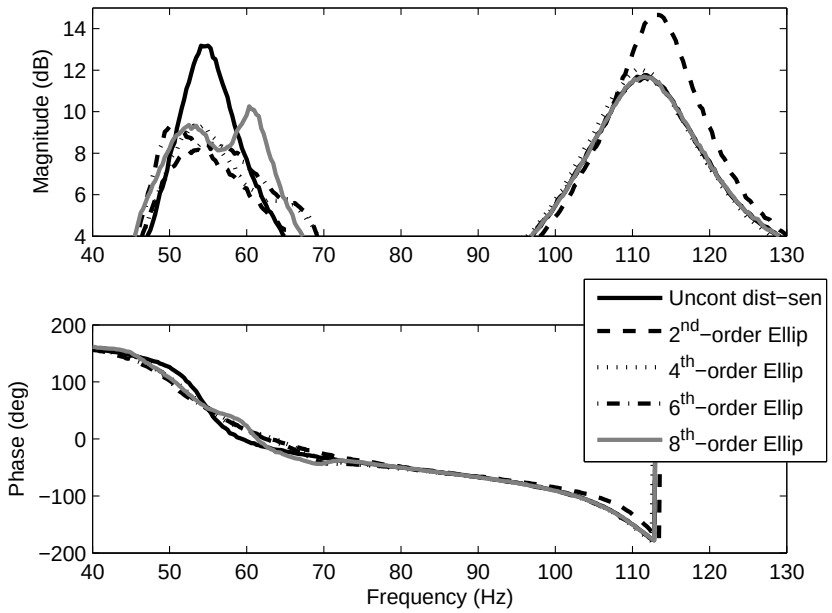

Figure 23: Experimental comparison of different order Elliptic controller responses.

As stated above, an advantage of using a feedback control approach is that the control is global. The reductions that are observed at the sensor location can also be observed elsewhere in the duct by moving the performance sensor, x_{perf}, to the various measurement ports shown in Figure 21. The results of moving x_{perf} along the duct axis at the various measurement ports is shown in Figure 26. Reductions of $5\,dB$ or more are observed for the first and last 3 measurement ports, respectively. Reductions of less than $5\,dB$ are noted for middle three measurement ports (P_4-P_6). The reductions that are observed are dependant

upon the placement of the microphone sensors. However, if there is no antinode present at the measurement location, energy will effectively be added at that control frequency. For collocated control of the fundamental duct mode, the measurement point $x_{perf} = P_5$ exhibits this phenomenon (indicated by the negative reductions).

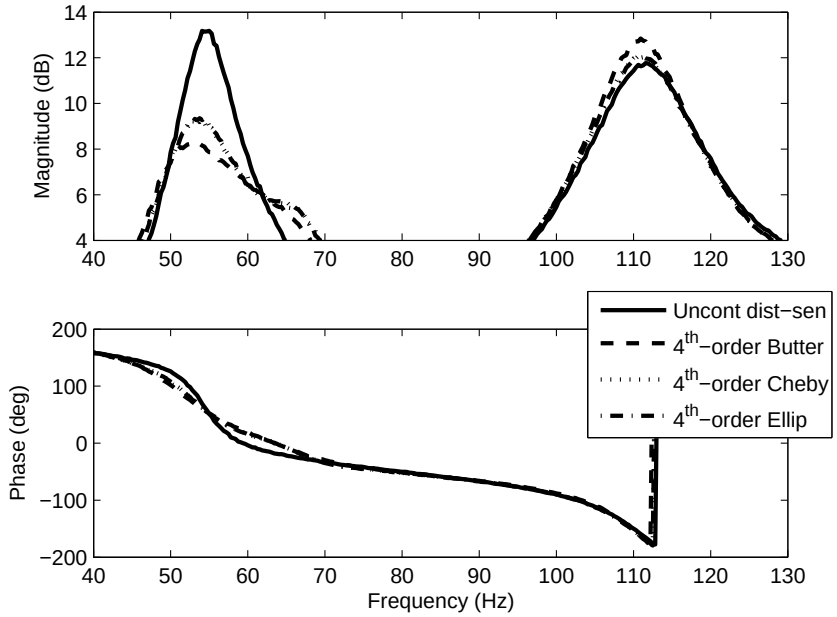

Figure 24: Experimental comparison of different design-type 4^{th}-order filter responses.

4.1.2 Non-Collocated Control

Another advantage of all-pass filter compensation is that non-collocated control can be achieved. The sensor microphone is moved to one of the 9 measurement ports along the duct axis shown in Figure 21. The performance microphone is used to examine the reductions at other measurement ports. Note the the transfer function paths discussed in Figure 7 still apply here. The disturbance and control paths are obtained in the same way as the collocated case. It is important to note that the non-collocated control/sensor path will be different from collocated one shown in Figure 22. However, the same procedure illustrated during control simulations in Section 3.3 is used to design the compensator.

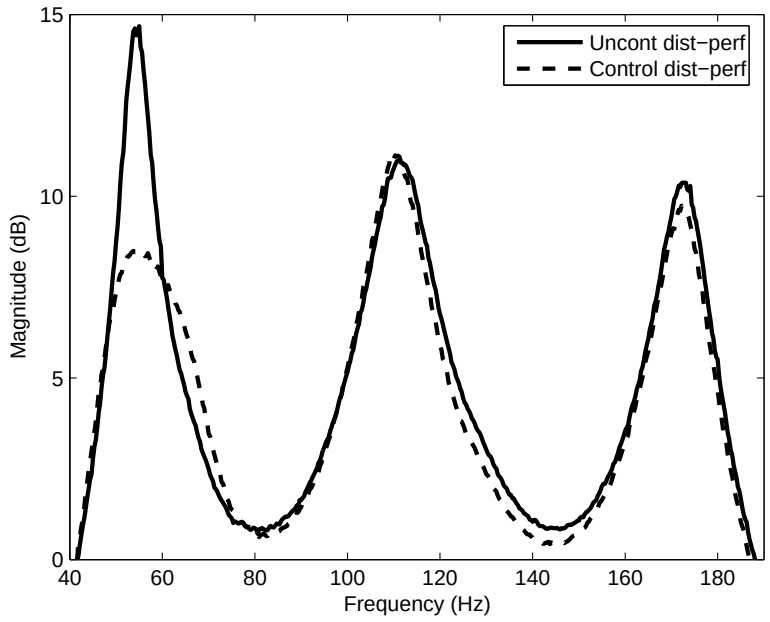

Figure 25: Single mode uncontrolled vs. controlled disturbance/performance path response.

To demonstrate non-collocated control, the sensor and performance microphones were moved to $x_{sen} = P_6$ and $x_{perf} = P_4$, respectively. The control/sensor path is examined in order to determine the phase at the control frequency, $\theta_c(\omega_c)$. A tuned 4^{th}-order Butterworth band-pass filter is used in series connection with a phase-compensating all-pass filter. Note that when x_{sen} is moved, the control path will no longer be minimum phase. However, the all-pass filter will bring the control/sensor path nearest multiple of 180^o at ω_c.

The results of relaxing the collocation requirement for the sensor/acuator pair can be seen in Figure 27, where $5\,dB$ of control is noted in the targeted 3^{rd} mode. Slight reduction is noted in the 2^{nd} mode, where a favorable phase contribution is introduced by the controller. Note that as with the collocated case, the control is demonstrated to be global by moving the performance sensor and any mode can be targeted. Again, the performance measurement can be taken at the other 7 port locations shown in Figure 21, and reductions are observed in the same manner as the the collocated case in Section 4.1.1.

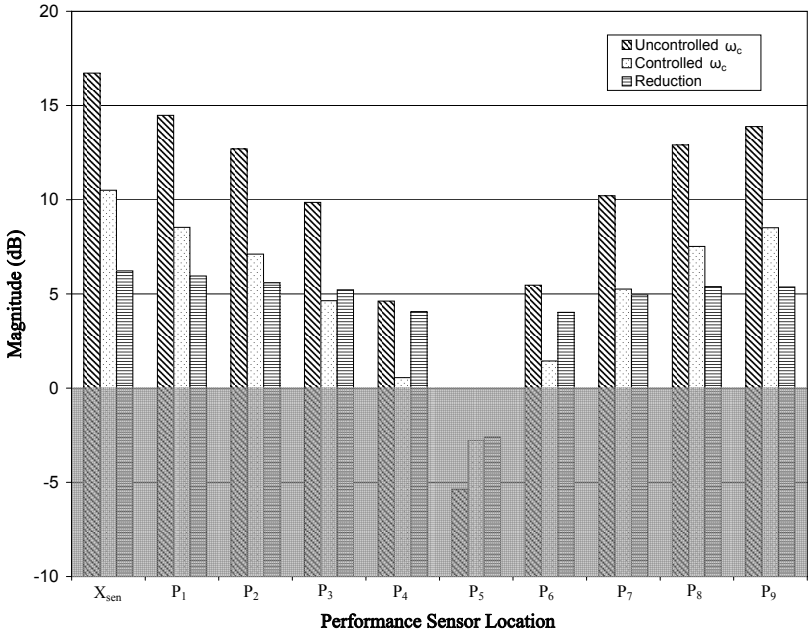

Figure 26: 1^{st} mode response along duct axis.

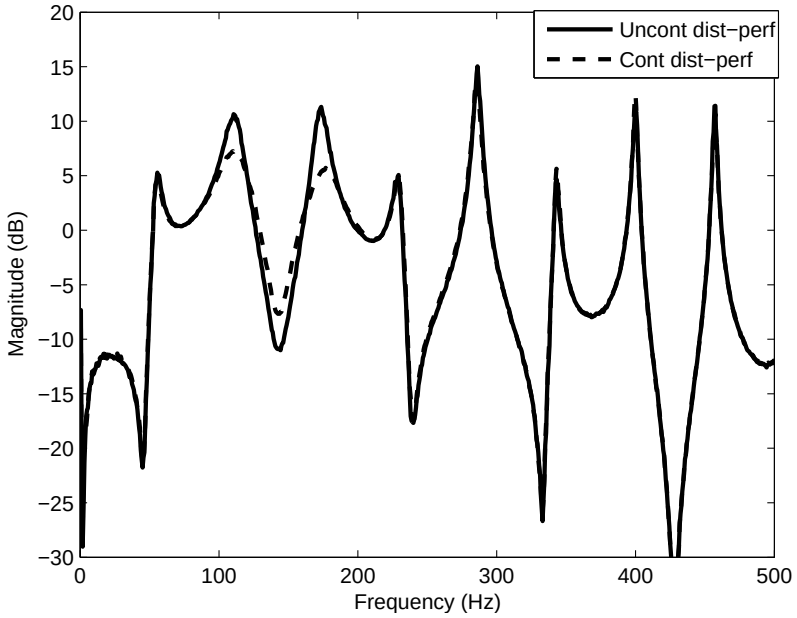

Figure 27: Non-collocated uncontrolled vs. controlled disturbance/performace path.

4.2 MULTIPLE MODE CONTROL

The procedure for controlling a single acoustic mode is now extended to multiple modes. Returning to Figure 22, the first 4 pressure modes are targeted for control shown in Table 3. Note that the acoustic loudspeaker and sensor microphone are collocated as shown by the control path response in Figure 22. The compensator is realized in the same manner as the single mode case. Each mode controller, which consists of a compensating filter and phase correction filter, is connected in parallel to form the multi-modal controller.

Table 3: First 4 pressure nodes of the acoustic duct.

Mode Number	*Frequency*
1	$54.37\,Hz$
2	$111.56\,Hz$
3	$172.5\,Hz$
4	$228.75\,Hz$

A key difference in the design approach is that the magnitude shaping band-pass filters must be added to the control/sensor path before the all-pass filters are designed. The experimental control/sensor path with (dashed line) and without (solid line) the 4^{th} order Butterworth band-pass filters are shown in Figure 28. The butterworth filter damping was determined in the manner shown during multi-modal control simulations. The phase required of the all-pass filter is determined from the dashed line in Figure 28 by examining the phase at the control frequencies. Figure 28 also shows the decoupling effect of the band-pass filters. The all-pass filters are implemented at each mode to achieve the desired 180^o of phase at each mode. Again, the same stability analysis that was performed on the single mode controller during control simulations is administered here.

The resonant filter comparison that was done for the experimental single mode controller is now extended to the multi-modal controller. The same discretization process that was used for the single mode controller comparison is used here. The highest sampling rate is chosen

based on the highest dynamic of the lowest mode targeted for control. The gain is kept constant for all controller designs comparisons. The damping for each modal compensator is the same for all comparisons and is chosen heuristically. A comparison of different order Chebyshev controllers in Figure 29 shows that the 4^{th}-order filters (dotted line) perform the best. Similar conclusions are made from different order Elliptic and Butterworth filter controller comparisons. 4^{th}-order Butterworth (dashed line), Chebyshev (dotted line), and Elliptic (dash-dotted line) filter controllers are compared in Figure 30. The Butterworth controller achieves slightly better control (around $1\,dB$ in controlled modes) than either the Elliptic or Chebyshev designs.

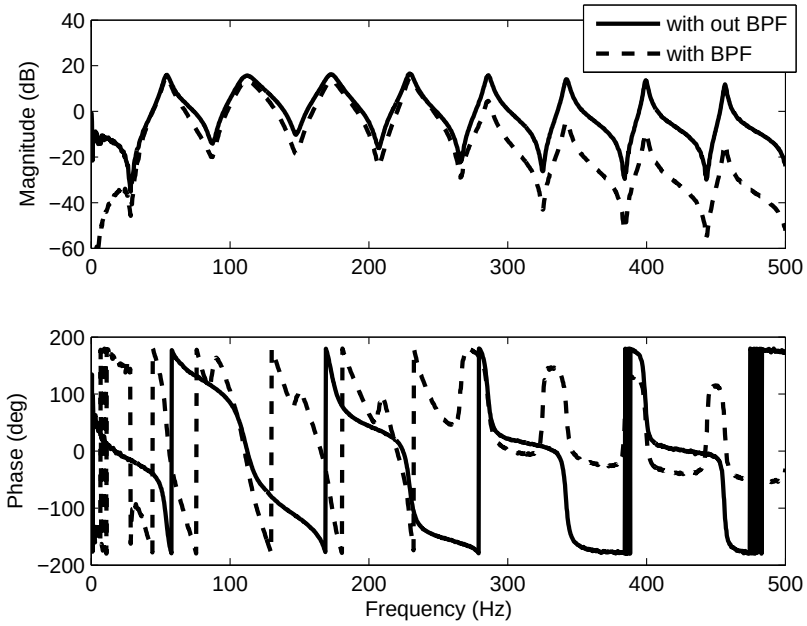

Figure 28: FRF of experimental control/sensor path with and without 4^{th}-order band-pass filters.

From the observations made above, the 4^{th}-order Butterworth filter compensator is chosen as the best performing controller. The performance sensor is placed at the measurement port closest to the collocated sensor microphone. The same Butterworth controller that was designed above during the resonant filter comparison is used here. However, filter gain and damping is chosen heuristically to ensure favorable results. The experimental demonstration

of multi-modal control on the disturbance/performance path for the first four modes of the rigid walled duct is shown in Figure 31. An average attenuation of $5 - 6\,dB$ is observed in the targeted modes with no appreciable spill-over.

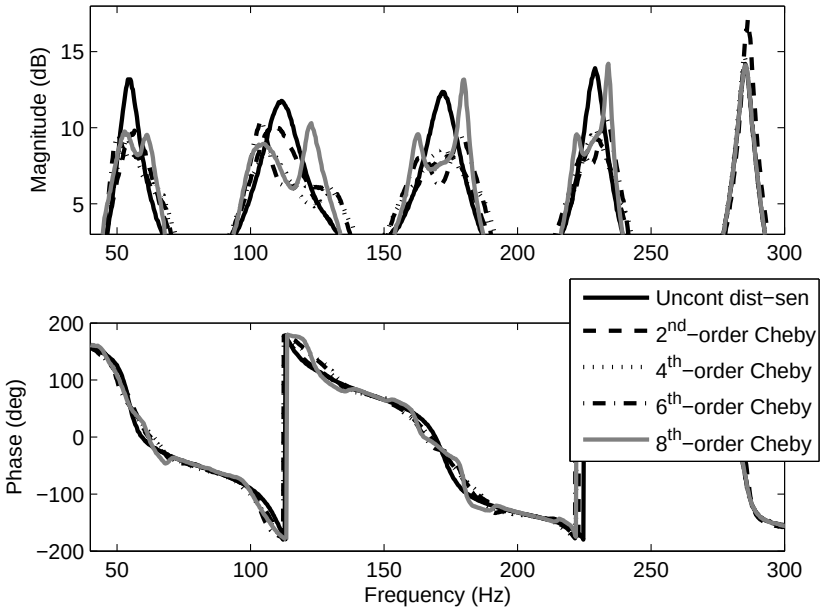

Figure 29: Experimental comparison of different order Chebyshev controller responses.

The multi-modal control is observed to be global, as shown in the single mode control case in Section 4.1.1. The reductions at the measurement ports along the duct axis for control of the first 4 duct modes can be seen in Figure 32. Note that Figure 32 exhibits reductions only, while Figure 26 also considers the uncontrolled and controlled response at the control frequency. Control is diminished as the performance sensor is moved toward the center of the duct. Again, if there is no mode present at ω_c, due the placement of x_{perf}, then energy is effectively added at that frequency.

The controller implemented in Figure 31 applied a single controller gain to each parallel connected compensator. However, note that excessive control is exhibited on mode 2, while only moderate control is shown on mode 1 and 4. Furthermore, the modal spacing and displacement of each acoustic mode is unique, thus each parallel compensator requires a specific gain. Care must taken when selecting gain applied to the controller, and consider

the observation made during the control simulations in Section 3.2.1. As gain is increased, compensator damping is decreased and phase interaction can occur. If too little gain is applied to the compensator, only modest control will be obtained. Note that only heuristical optimization was performed on the compensator. Improvements are expected if individually tailored gains are considered for each modal compensator, which is considered in the next chapter.

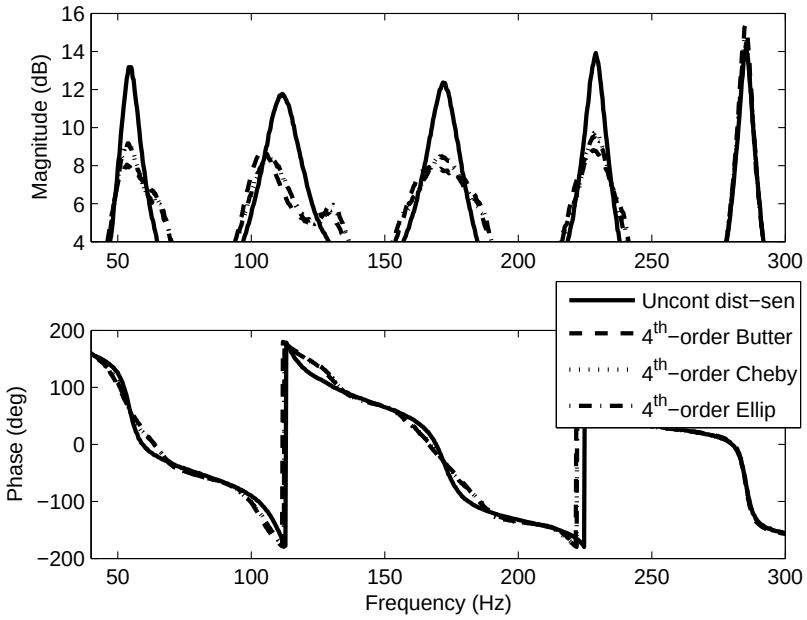

Figure 30: Experimental comparison of multi-modal Butterworth, Chebyshev, and Ellipitical controller responses.

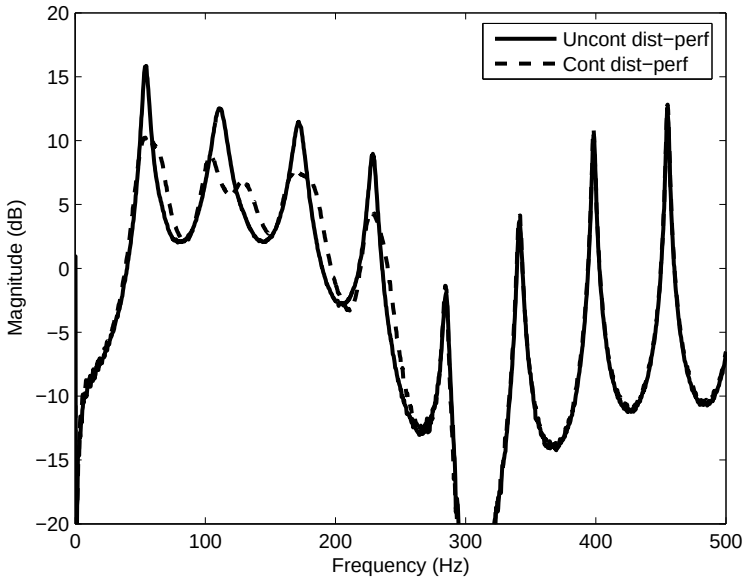

Figure 31: FRF of experimental multi-modal uncontrolled vs controlled disturbance/performance path.

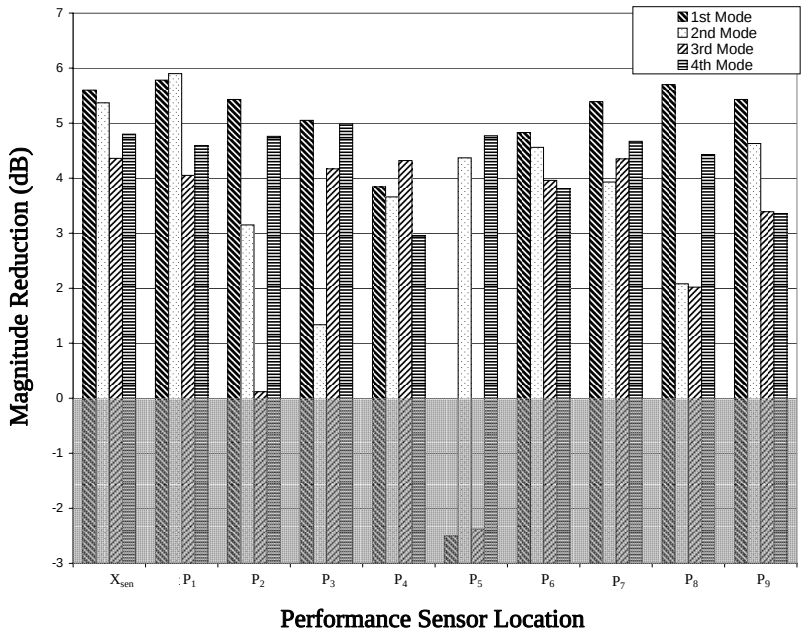

Figure 32: 1^{st} through 4^{th} mode reductions in response along duct axis.

5.0 ADAPTIVE CONTROL

In order to ensure that maximum attenuation is obtained by the controller, an adaptive algorithm is developed and discussed in this chapter [30]. Each duct mode shown in Figure [**?**] has unique damping and spacing requiring specific compensator parameters to achieve maximum reductions. Thus, each compensator must be adapted to the mode that it is controlling to ensure optimal results. Results shown in Section 4.2 demonstrated that having a single global gain value administered to the multi-modal controller yields only moderate control in some modes. Individual mode compensator gains are not individually optimized and are controlled by a single global gain. An adaptive controller has self-adjusting performance, and the added benefit of accomplishing controller modifications automatically.

There are four compensator parameters that can be considered for adaptation: control center frequency, damping, and gain. The control center frequency could be adapted by using a dot-product method to place the all-pass filter pole/zero locations [7]. Since ω_c will only need to be adapted if compensator damping is too low (i.e. phase interaction), its adaptation will not be examined. Compensator effective damping is determined by the bandwidth of the 4^{th} order Butterworth filters. Adapting the filter damping would require some form of pole/zero placement algorithm [23]. However, stability of the Butterworth Infinite Impulse Response (IIR) filter and feedback system would have to be analyzed [19]. The simplest parameter to adapt is the gain applied to each compensator, which will be addressed here. An adaptive algorithm is placed in the feedback path that guarantees proper gain values are applied to the resonant-mode controller.

In the following sections an adaptive algorithm will be developed and discussed. The adaptive algorithm updates gain values based on minimizing an error signal, and is applied to each parallel resonant mode compensator. After the algorithm is developed, it is applied to

the controller in simulations, and then demonstrated on the experimental test bed. Although adaptive single mode control can easily be shown, only adaptive multi-modal control will be examined in the following sections.

5.1 PRELIMINARY ADAPTIVE ALGORITHM

Both feedforward and feedback control approaches can be adaptive, but the way algorithms are employed for each case is typically different. Adaptive feedforward control relies on an adaptive filter that minimizes the residual error signal. In system identification approaches the adaptive feedforward algorithm updates filter coefficients, which creates an inverse plant model that has an output that is identical to the primary disturbance. On the other hand, adaptive feedback system have two feedback loops associated with the controller. The "inner loop" contains the controller, and the "outer loop" that consist of the adaptive algorithm that feeds back information to update the controller. Many feedback control approaches are transformed into feedforward schemes using a plant model and an internal mode controller (IMC)[6]. However, this method requires system identification which can be computationally intensive.

There are many adaptive algorithms that have been applied to ANC systems [20], the most popular of which is the least mean square (LMS) algorithm. The LMS algorithm minimizes the mean square value of the error signal (MSE), and is based upon steepest descent. In adaptive filter applications, the LMS algorithm updates filter weights such that the error signal is attenuated. The same approach can be used to optimize the gain applied to the resonant mode control system. By using steepest decent of the MSE, gain values applied adaptively to the control system will ensure that signal energy is reduced [19, 32].

The proposed adaptive algorithm uses a heuristic approach, which is similar to steepest decent search method to reduce the MSE. The adaptive algorithm is implemented in the same manner as shown in [15]. A flow diagram of the proposed adaptive algorithm to be used in conjunction with the resonant mode controller is seen in Figure 33. The design process for the compensator does not change for the adaptive case, a tuned band-pass filter with all-pass phase correction is still used. A cost function is computed for both the current

gain value ($C_1 = f(K)$) and for the gain that has been perturbed by δk ($C_2 = f(K + \Delta k)$). The gradient of the cost function is determined as:

$$\frac{\partial C}{\partial K} \approx \frac{C_2 - C_1}{\Delta k}. \tag{5.1}$$

Equation 5.1 could be implemented directly for steepest descent approach, however as the reader will see, a heuristic approach like [15] is employed here. Note that by adapting the gain, the damping is also adapted. Although pole-zero locations are determined during controller design, the gain is adapted along root locus lines which determine damping and natural frequency as shown in Figure 34.

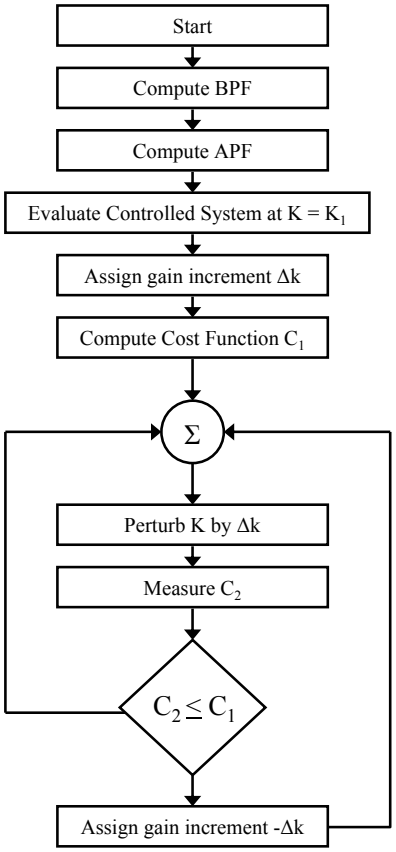

Figure 33: Flow diagram of the adaptive algorithm.

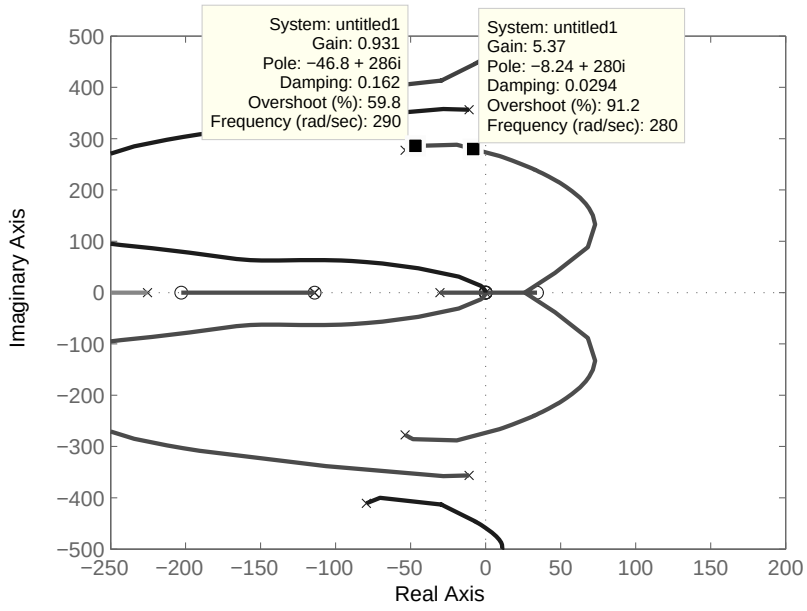

Figure 34: Root locus plot of 4-mode controller on the control/sensor path

The adaptive algorithm is configured in the feedback path of the resonant mode controller. A block diagram showing the connections of the adaptive controller is shown in 35. Note that all parallel-connected compensators are embedded in the Controller, $H_{comp}(n)$. The error signal, $e(n)$, is determined by filtering the sensor signal, $s(n)$, using Butterworth band-pass filters to localize signal error computations at ω_c. The error signal perturbed by K is defined as:

$$e(n, K) = (H_{ds}(n, K) * d(n) + H_{cs}(n, K) * c(n)) * BPF. \tag{5.2}$$

Note that the band-pass filters used to compute the error signal are different than the ones used in the controller. The error signal is formed through the convolution of the disturbance and control signals with the disturbance and control paths, respectively. The cost function perturbed by gain K is based on squared error and is defined as:

$$C_1 = E[e(n, k)^2]. \tag{5.3}$$

To determine if the algorithm is converging, a the second cost function is computed with the added gain, Δk. The same derivation can be used to find the cost function perturbed by Δk as was shown above, and is expressed as:

$$C_2 = E[e(n, K + \Delta k)^2]. \tag{5.4}$$

The localized error signal is used by the adaptive algorithm to compute the cost functions C_1 and C_2 for each mode. The gain applied to each compensator is determined by the localized cost functions described in Figure 33. Note that the adaptive gain is in series with each mode compensator, and is summed to form the control signal, $c(n)$. Since both the feedback controller and adaptive algorithm are in the feedback path, the same stability analysis that was shown in Section 3.3 is used here. Although stability is not guaranteed, by minimizing MSE the adaptive algorithm should converge and produce a stable controller. Efforts are now concentrated on simulating and experimentally testing the adaptive algorithm on the acoustic duct.

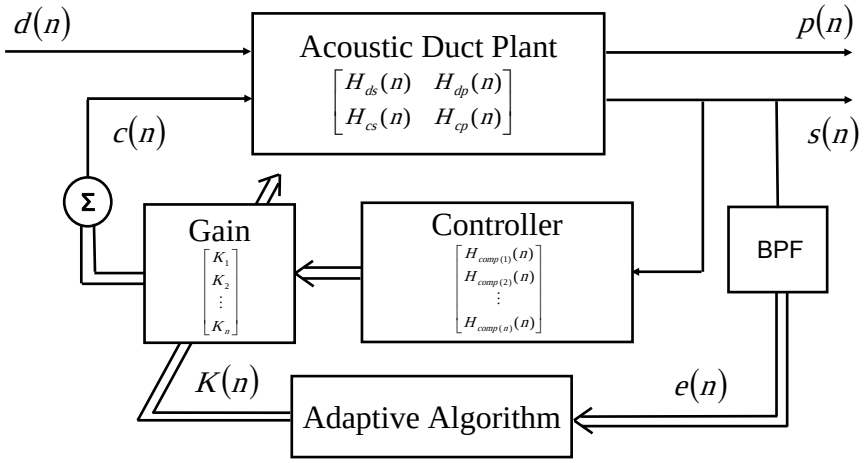

Figure 35: Block diagram of the adaptive feedback controller.

5.2 ADAPTIVE CONTROL SIMULATION

A simulation of the 4-mode controller with adaptive gain is now considered. The 4^{th} order band-pass and all-pass filter compensators are developed in the same fashion as described in Section 3.4. To be consistent with the model developed in Chapter 3, the adaptive algorithm was first designed and implemented using standard programming in MATLAB^{TM} . However, it was found that simulations done using MatLab^{TM} Simulink software package allowed for indefinite and less computationally intensive simulations. The Simulink models that were used in simulations can be seen in Appendix A. Although initially there is no gain applied to the system, perturbation values were chosen heuristically to ensure that the algorithm would converge.

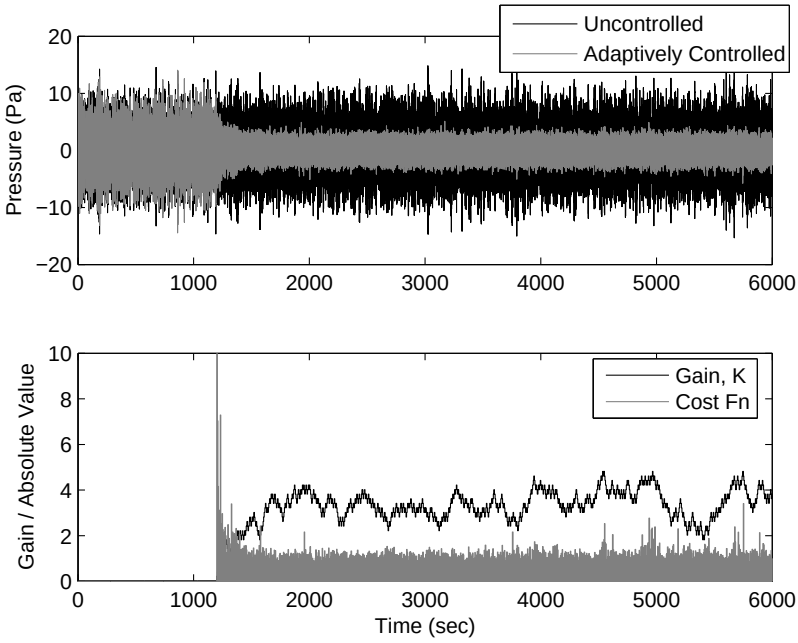

Figure 36: Uncontrolled and adaptively controlled disturbance/sensor signal.

The disturbance/sensor path signal with and without the adaptive algorithm applied can be seen in Figure 36. It is observed that for the first 2000 seconds there is no control applied to the system. After that point in time, adaptive control is turned on and the signal is attenuated. Also observed from Figure 36 the convergence of the adaptive algorithm's gain and cost function is observed to take approximately 500 seconds. An average reduction of

$7 - 8\,dB$ is noted in Figure 37 on the first 4 modes of the analytic disturbance/performance path with adaptive control applied.

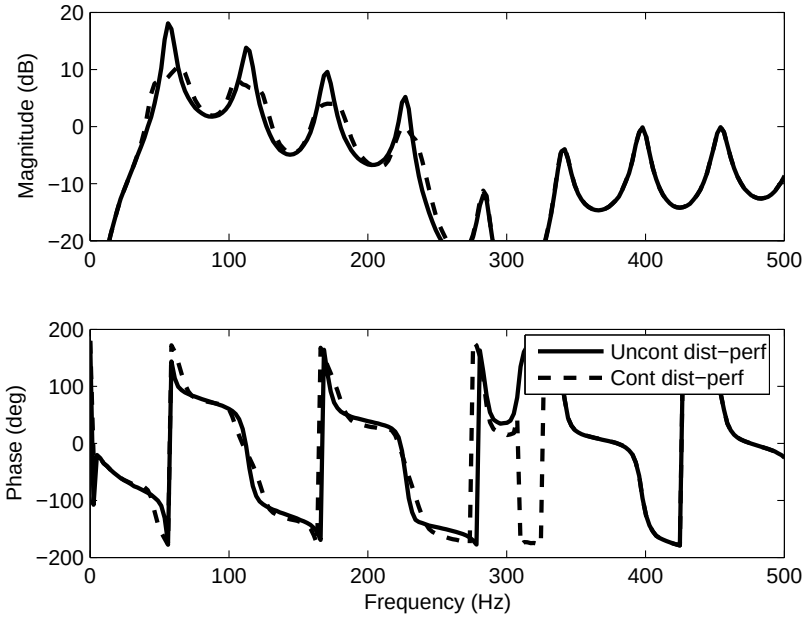

Figure 37: Response of adaptive uncontrolled and controlled disturbance/performance path.

5.3 EXPERIMENTAL ADAPTIVE CONTROL DEMONSTRATION

In order to verify the adaptive algorithm, a compensator with the adaptive gain algorithm is developed to control the first four acoustic modes on the experimental test bed shown in Figure 20. As with the other experimental demonstrations, the input to the disturbance speaker was $500\,Hz$ white noise. The disturbance/performance path was measured by placing the performance microphone x_2 at P_1 in Figure 21. The control path was determined by the collocated microphone placed at x_1 in Figure 4. Again, all controller components, including the adaptive gain, was implemented on the Dspace $DS1104$ R&D Board using the MatLab^{TM} RTI.

The controller was developed in the same manner as discussed in the previous section. The resonant 4-mode compensator consists of 4 Butterworth band-pass filters with 4 all-pass

filters tuned at the target frequency of each mode. Filter damping is unique to each compensator, and is chosen in a heuristic manner shown in chapters 3 and 4. The disturbance/sensor path is processed by the DSP where the adaptive algorithm and controller are implemented to create the control path. The recursive algorithm updates gain applied to each parallel connected compensator so that the error signal energy is minimized. The Simulink Block Diagrams that were used to implement the adaptive control can be seen in Appendix B.

The adaptive uncontrolled and controlled system response is plotted in Figure 38. A balance between filter damping and gain is achieved by reducing the sensor signal error. An average reduction of $6 - 7\,dB$ has been observed in each of the controlled modes, with improvements of $3\,dB$ in the fist mode and $2\,dB$ fourth mode. Unlike the non-adaptive case, the adaptive resonant mode controller achieves maximum control at each mode. Since the MSE signal is minimized by the algorithm and the gain for each mode is individually tailored, this is the best possible reduction that can be obtained with the given filter damping parameters. The adaptive algorithm also guarantees that the modes will not "split" from excess gain [5], and create a worse modal response at shifted frequencies.

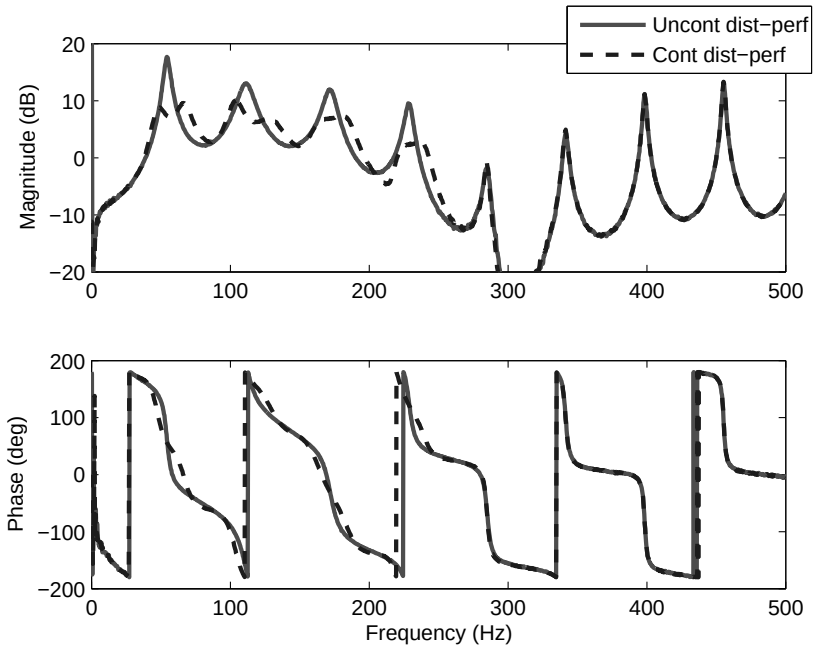

Figure 38: Experimental uncontrolled vs adaptively controlled disturbance/performance response.

6.0 CONCLUSIONS AND FUTURE WORK

Several refinements have been incorporated into a new type of acoustic control system that uses positive position feedback (PPF) with damped, resonant filters [4]. Past studies have concentrated on the design and component architecture of PPF applied to acoustic systems. By examining design variables, insight has been gained into creating a more efficient resonant mode controller. Realizing the controller using a digital signal processor (DSP) board allowed for easy examination of the design parameters, and greatly facilitated control beyond two modes. System refinements were first simulated using an analytical duct model, and then demonstrated on the experimental test bed. Finally, a adaptive algorithm was developed and implemented to update gain values applied to the multi-modal control filters.

The type of resonant filter used in the compensator has a profound impact system performance for both single and multi-modal control. Band-Pass filters, rather than low-pass filters, were found to give improved results when considering multi-modal control. Band-pass filters provide magnitude roll-off at both high and low frequencies around ω_c, while also allowing for a sharper phase shift. This was found to help de-couple phase interactions between controlled and uncontrolled modes. Three types of higher-order band-pass filters were investigated: Butterworth, Chebyshev, and Elliptic. Through control system simulations, it was found that 4^{th} Butterworth filters provided roll-off of $\pm 40\, dB/dec$ and maximally flat pass-band at the control frequency. Thus, Butterworth filters provide maximum attenuation, while also limiting phase interaction of controlled/uncontrolled modes. The band-pass filters alone cannot achieve an "out of phase" signal and requires the use of an all-pass phase-correction filter, as shown in previous studies [3]. The resonant controller demonstrated reductions of $5 - 6\, dB$ on the first four modes of the rigid-walled duct test bed.

Placement of the microphone sensors determine the transfer function paths of the control system. These system conventions were clarified to gain greater insight into performance and stability of the controller. Since the resonant mode controller is a non-minimum phase system, controller stability can not be guaranteed. However, Nyquist stability criterion was used to evaluate the effects gain on controller performance and stability. The ability of the phase compensation method to compensate a non-minimum phase system also allows for the collocation requirement of standard PPF to be relaxed. Non-collocated was experimentally demonstrated by moving the sensor microphone away from the control speaker, and $5\,dB$ of attenuation was noted.

Test were conducted to determine whether the type of control that being administered is global or local. Global reduction was confirmed by utilizing a performance sensor with the 9 equally spaced duct measurement ports along the duct axis and comparing uncontrolled vs. controlled responses. Attenuation is achieved at each measurement port, as long as their is a pressure node present at the control frequency. Speaker power, acceleration, and velocity was also measured for controlled and uncontrolled cases to ensure that the disturbance speaker was unimpeded.

An adaptive algorithm is presented to ensure that proper gain levels are applied to each mode of the controller. Each acoustic mode of the duct is unique, thus requiring specific compensator gain and damping. The adaptive algorithm updates gain values based on the mean square error (MSE) of the pressure signal that is fed back to the controller. The adaptive controller assures that maximum reduction is obtained, given the damping present in the compensator(s). An average adaptive control of $6 - 7\,dB$ is observed on the experimental test bed. The adaptive controller also has the added benefit of being self adjusting, making it applicable to other closed cavity noise problems.

Compensator damping has the greatest impact on the performance of the resonant control system. Compensator damping is determined by the bandwidth of the Butterworth band-pass filter [31, 22]. Although effects of the compensator damping was investigated heuristically, some important observations were made. The amount of control and phase interaction is proportional to the amount of compensator damping. Optimization of compensator damping could be achieved in the same manner as tuned absorbers in structures.

However, parallels between acoustic (PPF) and mechanically tuned absorbers must first be investigated.

Future work will further investigate the parameters and optimization of acoustic PPF. The most important of these design parameters is the compensator damping and control frequency. A compensator with adaptive damping and control frequency would achieve maximum reductions without causing phase shifts. The algorithm could use true steepest decent to place the poles/zeros of the compensator. However, the theoretical limits of stability must be examined in order to achieve a better defined control system. This would lead to easier adaptation of other system parameters. In order to develop a better adaptive controller, the stability of the adaptive feedback gain must be investigated. To better compare results, a relationship between Helmholtz resonators, mechanically tuned absorbers, and acoustic PPF using all-pass phase compensation must be defined. Realizing such a relationship would allow for optimization techniques already used for mechanically tuned absorbers [28]. Finally, using a mix of filter types on different modes could lead to a better control system.

APPENDIX A

MATLAB SIMULINK^{TM} CODE FOR ADAPTIVE CONTROL SIMULATIONS

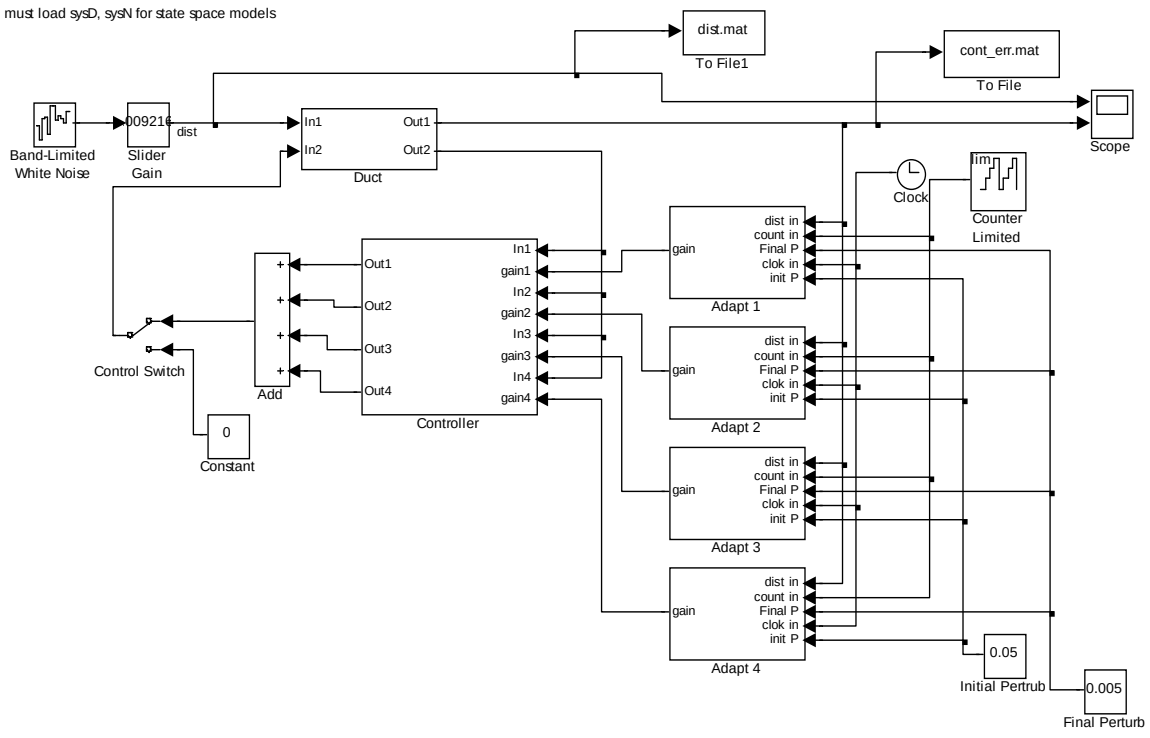

Figure 39: Simulink code for the simulated adaptively controlled system.

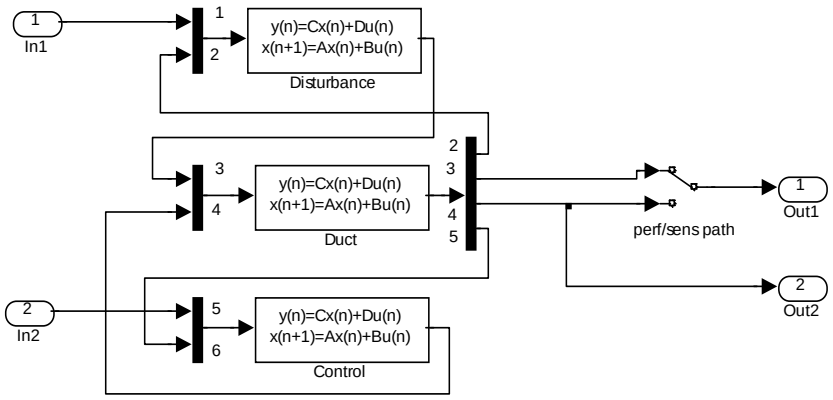

Figure 40: Simulink code for the simulated acoustic duct sub-system.

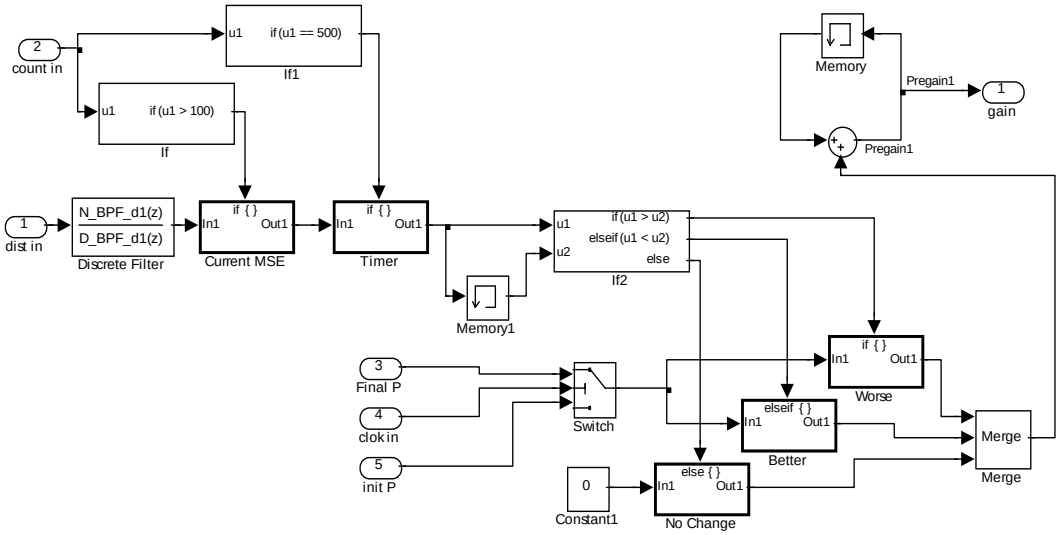

Figure 41: Simulink code for the simulated adaptive algorithm sub-system.

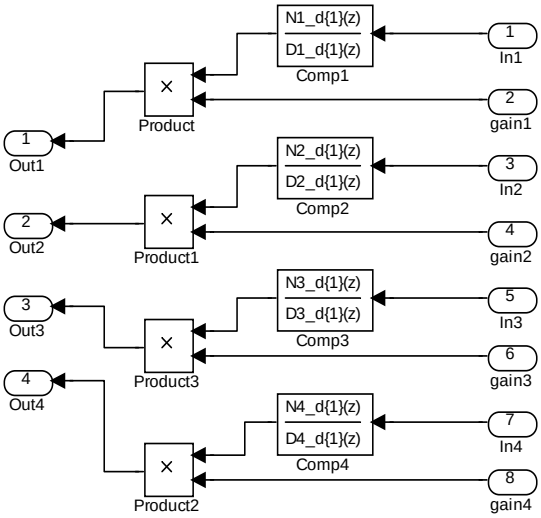

Figure 42: Simulink code for the simulated controller sub-system.

APPENDIX B

MATLAB SIMULINK^{TM} CODE FOR ADAPTIVE CONTROL EXPERIMENTAL DEMONSTRATION

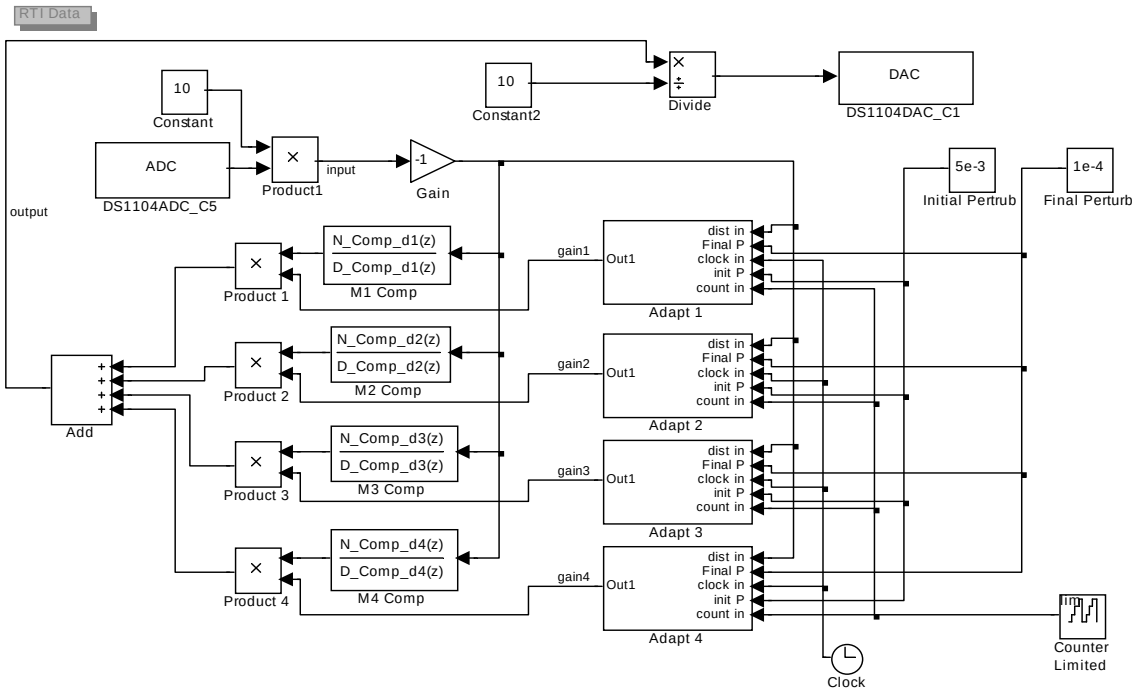

Figure 43: Simulink code for the experimental adaptive controller.

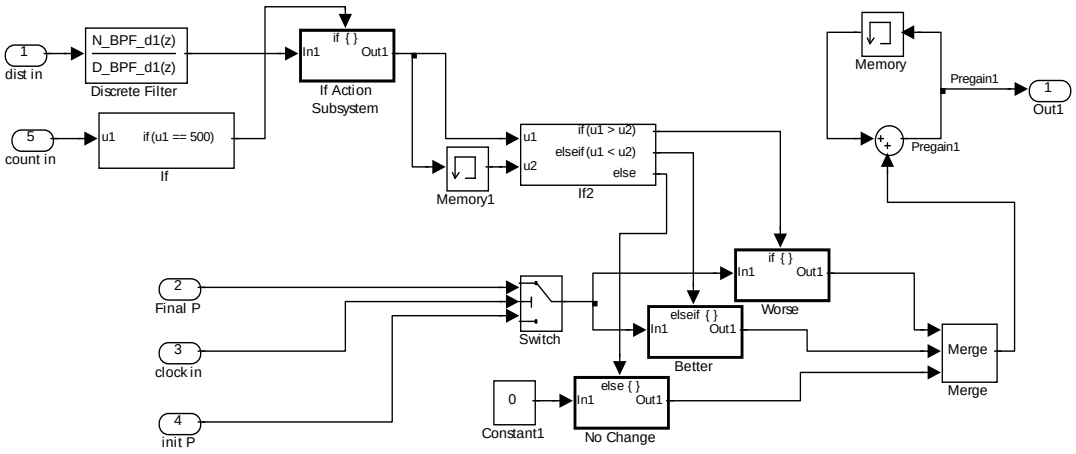

Figure 44: Simulink code for the experimental adaptive algorithm sub-system.

BIBLIOGRAPHY

[1] David A. Bies and Colin Hansen. *Engineering Noise Control: Theory and Practice*. Taylor and Francis Group, New York, 2003.

[2] C. B. Birdsong and C. J. Radcliffe. A compensated acoustic actuator for system with strong dynamic pressure coupling. *JVA*, 121:89–94, January 1999.

[3] J. B. Bisnette, J. S. Vipperman, and D. D. Budney. Active noise control using phase-compensated, damped resonant filters. *ASME IMECE*, (2003-41831), November 15-21 2003. Washington, D.C.

[4] Jesse B. Bisnette. Active noise control using modally tuned phase-compensated filters. Master's thesis, University of Pittsburgh, 2003.

[5] J. P. den Hartdog. *Mechanical Vibrations*. McGraw-Hill Book Company, New York, 4th edition, 1956.

[6] S. J. Elliot. *Signal Processing for Active Control*. Academic Press, New York, 2001.

[7] S. J. Estve and M. E. Johnson. Reduction of sound transmitted into a composite cylinder using distributed vibration absorbers and helmholtz resonators. *Journal of the Acoustical Society of America*, 112(6):2040–2048, 2002.

[8] F. J. Fahy and C. Schofield. A note on the interaction between a helmoltz resonator and an acoustic mode of an enclosure. *JVA*, 72(3):365–378, April 1980.

[9] J. L. Fanson and T. K. Caughey. Positive position feedback control for large space structures. *AIAA Journal*, 28(4):717–724, April 1990.

[10] K. M. Farinholt and D. J. Leo. Acoustic modeling and control of conical enclosures. *JVA*, 125(1):2–11, 2003.

[11] Woon S. Gan and Sen M. Kuo. An integrated audio and active noise control headsets. *IEEE*, 48(2):242–247, May 2002.

[12] C. J. Goh and T. K. Caughey. On the stability problem caused by finite actuator dynamics in the collocated control of large space structures. *Int. J. Control*, 41(3):787–802, 1985.

[13] Edison J. Hahn and T. F. Edgar. A note on stability analysis using bode plots. *Chemical Engineering Education*, 35(3):208–11, Summer 2001.

[14] Colin H. Hansen. *Understanding Active Noise Cancellation*. Spon Press, New York, 2001.

[15] R. J. Bernhard J. M. De Bedout, M. A. Franchek and L. Mongeau. Adaptive-passive noise control with self-tuning helmholtz resonators. *JSV*, 202(1):109–123, October 1997.

[16] A. G. Kelkar and H. R. Pota. Robust broadband control of acoustic duct. *IEEE*, 1:273–278, September 2000.

[17] Lawrence E. Kinsler. *Fundamental of acoustics*. Wiley, New York, 1982.

[18] Theodore M. Kostek. Combining adaptive-pasive and fully active noise control in ducts. *ASME Noise Control and Acoustics Division*, 24:293–298, November 1997.

[19] Sen M. Kuo and Dennis R. Morgan. *Active Noise Control Systems*. John Wiley and Sons, New York, 1996.

[20] Sen M. Kuo and Dennis R. Morgan. Review of DSP algorithms for active noise control. *IEEE ICCA*, (0-70803-6562-3/00), September 25-27 2000. Anchorage, Alaska.

[21] Steven A. Lane and Robert L. Clark. Dissipative feedback control of a reverberant enclosure using a constant volume velocity source. *JVA*, 120(3):987–993, 1998.

[22] M. D. Lutovac, D. J. Tosic, and B. L. Evans. *Filter Design for Signal Processing*. Prentice Hall, New Jersey, 2001.

[23] M. McEver and D. J. Leo. Autonomous vibration suppression using on-line pole-zero identification. *JVA*, 123:487–495, October 2001.

[24] Jerzy Moascianski and Zbigniew Ogonowski. *Advanced control with Matlab and Simulink*. Prentice Hall, Ellis Horwood, London, 1995.

[25] W. Neise and G.H. Koopmann. Reduction of centerifugal fan noise by use of resonators. *Journal of Sound and Vibration*, 73(2):297–308, November 1980.

[26] Young C. Park and Scott D. Sommerfeldt. Global attenuation of broadband noise fields using energy density control. *Journal of the Acoustic Society of America*, 101:350–359, January 1997.

[27] H. R. Pota and A. G. Kelkar. Modeling and control of acoustic ducts. *Transactions of the ASME*, 213:2–10, January 2001.

[28] Singiresu S. Rao. *Mechanical Vibrations*. Prentice Hall, Upper Saddle River, New Jersey, 4th edition, 2004.

[29] A. K. Smith, J. B. Bisnette, J. S. Vipperman, and D. D. Budny. Active noise control using phase-compensated, damped resonant filters. *JVA*, 2004. Accepted for publication.

[30] Adam K. Smith, Jeffrey S. Vipperman, and Daniel D. Budny. Adaptive resonant mode acoustic controller. *IMECE*, 2005. Accepted For Publication.

[31] M. E. Valkenburg. *Analog Filter Design*. Holt and Rinehart and Winston, Philadelphia, 1982.

[32] Bernard Widrow and Samuel D. Stearns. *Adaptive Signal Processing*. Prentice Hall, Englewood Cliffs, New Jersy, 1985.